

Effect of mixed convection on laminar vortex breakdown in a cylindrical enclosure with a rotating bottom plate

João N. N. Quaresma^{a,b,c,*}, Carlos C. S. da Cruz^{a,d}, Neil Cagney^{e,f},
Renato M. Cotta^{e,g}, and Stavroula Balabani^c

^a Graduate Program in Natural Resource Engineering in the Amazon, PRODERNA/ITEC/UFPA, Universidade Federal do Pará, 66075-110, Belém, PA, Brazil.

^b School of Chemical Engineering, FEQ/ITEC/UFPA, Universidade Federal do Pará, 66075-110, Belém, PA, Brazil.

^c Department of Mechanical Engineering, University College London, UK, WC1E 7JE

^d Science and Technology Program, UFOPA, Universidade Federal do Oeste do Pará, 68040-470, Santarém, PA, Brazil.

^e Mechanical Engineering Department, POLI & COPPE, Universidade Federal do Rio de Janeiro, Cx. Postal 68503, Cidade Universitária, Rio de Janeiro, RJ, Brazil, 21945-970

^f School of Engineering and Materials Science, Queen Mary University of London, E1 4NS, London, UK

^g General Directorate of Nuclear and Technological Development, DGDNTM, Brazilian Navy, Ministry of Defense, RJ, Brazil

* Corresponding author: João N. N. Quaresma (quaresma@ufpa)

Abstract

Vortex breakdown plays a central role in the performance of countless rotating machinery applications, many of which contain thermal gradients either inadvertently or by design. The effect of thermal gradients on vortex breakdown and further flow development in a cylindrical domain with a rotating bottom plate is examined using the Generalized Integral Transformation Technique (GITT) with a streamfunction-only formulation. A thermal gradient is imposed in the axial direction, such that the buoyancy forces oppose the base flow driven by the rotation of the lower plate, i.e. the temperature difference acts to stabilize the flow. The hybrid numerical-analytical approach is shown to accurately capture vortex breakdown phenomena for a variety of conditions involving single, double and triple recirculation bubbles. The buoyancy forces – expressed in terms of the Richardson number (Ri) – act to suppress vortex breakdown in all cases examined and led to a series of flow transitions with increasing Ri , characterized by the appearance of a stratified structure with multiple fluid layers. These flow transitions have a significant impact on the overall performance of the system. The torque coefficient decreases with Ri , compared to the base (isothermal) case following an empirical power law relationship, which is independent of Reynolds number, aspect ratio or number of fluid layers present. Flow stratification suppresses the transport of angular momentum; azimuthal velocity is shown to decline exponentially in the regions where layering occurs, accompanied by a sharp reduction in the Nusselt number, as fluid layers act to insulate the upper plate.

Keywords: Vortex breakdown; Swirling flow; Navier-Stokes and energy equations; Mixed convection; Integral transforms; Cylindrical cavity.

Nomenclature

A_{ij}	integral coefficient given by Eq. (44)
B_{ijk}	integral coefficient given by Eq. (44)
C_{ijk}	integral coefficient given by Eq. (45)
C_T	torque coefficient
D_{ijk}	integral coefficient given by Eq. (45)
E_{ijk}	integral coefficient given by Eq. (46)
\bar{f}_i	transformed boundary condition given by Eq. (49)
F_{ij}	integral coefficient given by Eq. (46)
Fr	Froude number ($=\omega^2 R/g$)
g	gravity acceleration (m/s^2)
\bar{g}_i	transformed boundary condition given by Eq. (49)
G_{ijk}	integral coefficient given by Eq. (47)
Gr	Grashof number ($=\beta \Delta T^* g R^3/\nu^2$)
h	aspect ratio ($=H/R$)
H	cavity height (m)
h_c	heat transfer coefficient (W/m^2K)
\bar{h}_i	integral coefficient given by Eq. (52)
H_{ijk}	integral coefficient given by Eq. (47)
I_{ijk}	integral coefficient given by Eq. (48)
J_{ijk}	integral coefficient given by Eq. (48)
k	fluid thermal conductivity (W/mK)
L_i	normalization integral for the streamfunction field
M_i	normalization integral for the azimuthal velocity component
N	truncation order
NF, NV, NT	truncation orders for the streamfunction, azimuthal velocity component, and temperature expansions, respectively
N_i	normalization integral for the temperature field
Nu_0, \bar{Nu}_0	local and average Nusselt numbers at the bottom, respectively
Nu_h, \bar{Nu}_h	local and average Nusselt numbers at the top, respectively
P^*, P	pressure field, dimensional (N/m^2) and dimensionless, respectively
Pr	Prandtl number ($=\nu/\alpha$)
q''	heat flux at the upper plate (W/m^2)
r^*, r	radial coordinate, dimensional (m) and dimensionless, respectively
R	cylinder radius (m)
Ra	Rayleigh number ($=\beta \Delta T^* g R^3/\nu\alpha=GrPr$)
Re	Reynolds number ($=\omega R^2/\nu$)
Ri	Richardson number ($=\beta \Delta T^* g/R\omega^2=Gr/Re^2$)
T^*, T	temperature field, dimensional (m) and dimensionless, respectively
T_0	reference temperature (K)
\bar{T}_i	transformed temperature
v_r^*, v_r	radial velocity component, dimensional (m/s) and dimensionless, respectively
v_z^*, v_z	axial velocity component, dimensional (m/s) and dimensionless, respectively
v_θ^*, v_θ	azimuthal velocity component, dimensional (m/s) and dimensionless, respectively
$\bar{v}_{\theta,i}$	transformed azimuthal velocity component
$v_{\theta,m}$	mean azimuthal velocity at a given depth
X_i	eigenfunctions for the streamfunction expansion
Y_i	eigenfunctions for the azimuthal velocity component expansion
z^*, z	axial coordinate, dimensional (m) and dimensionless, respectively

Greek Letters

α	fluid thermal diffusivity (m^2/s)
β	coefficient of thermal expansion of the fluid (K^{-1})
β_i	eigenvalues for the temperature expansion
γ_i	eigenvalues for the streamfunction expansion
Γ_i	eigenfunctions for the temperature expansion
ΔT^*	temperature difference between the top and the bottom plates (K)
θ	angular coordinate
λ_i	eigenvalues for the azimuthal velocity component expansion
μ_i	eigenvalues for the temperature expansion
ν	kinematic viscosity of fluid (m^2/s)
ρ	fluid density (kg/m^3)
$\bar{\Psi}_i$	transformed streamfunction
Ψ	streamfunction field
ω	characteristic rotational velocity (s^{-1})
ω_b	rotational velocity of the bottom disk (s^{-1})
ω_θ	azimuthal vorticity component (s^{-1})

Subscripts and superscripts

i,j,k	orders from eigenvalue problems
*	dimensional quantities
—	transformed quantities

1. Introduction

Swirling flows occur throughout nature, such as tornadoes and hurricanes, and in countless industrial applications, including heat exchangers, combustion systems, bioreactors, separation, aeronautics, and spray drying devices. Such flows are characterized by the formation of a central vortex which has the tendency to breakdown, forming a recirculation region along the vortex core that strongly affects the overall application performance. Vortex breakdown (VB) has been the subject of extensive research over the past five decades and has been the topic of a number of reviews [1-5].

Vortex breakdown can occur as an unsteady or steady process; either by the unravelling of the vortex core to form a spiral or double helix [5], or via the formation of stationary, axisymmetric recirculation bubbles along the vortex axis [6], respectively. The unsteady mode tends to occur in unconfined flows (as in aeronautics) [5], while the axisymmetric mode often dominates in confined flow, especially when there is no mean flow in the axial direction [4,7]. A cylindrical container in which one end plate is rotating at a speed, ω , and the other is fixed, is the simplest geometry in which axisymmetric vortex breakdown occurs and is directly relevant to many industrial applications. The system can be characterized using two non-dimensional groups; the Reynolds number, $Re = \omega R^2/\nu$ (where R is the cylinder radius and ν is the kinematic viscosity of the fluid) and the aspect ratio, $h = H/R$ (where H is the cylinder height). Escudier [6] performed a series of flow visualization experiments in order to characterize the different regimes of vortex-breakdown, including stable flow (no breakdown), axisymmetric breakdown with one, two or three bubbles present, and unsteady oscillations. For $Re \leq 2500$, the unsteady instability was not observed. As the Reynolds number is increased further, the flow becomes unsteady and eventually chaotic ($Re \sim 10^4$) [8]. The breakdown and the appearance of the different regimes is thought to depend strongly on the distribution of azimuthal vorticity [9,10] and only occurs for $h \sim O(1)$ [9]. Sorensen et al. [11] studied the swirling flow between a rotating lid and a stationary cylinder experimentally using laser-based flow diagnostics, namely Particle Image Velocimetry (PIV) and Laser Doppler Anemometry (LDA). The onset of three-dimensional flow behavior was measured and a detailed mapping of the transition scenario from steady and axisymmetric flow to unsteady and three-dimensional flow was provided, including table of neutral and critical Reynolds numbers obtained from LDA measurements carried out in the range $h \in [1.0, 3.5]$ with a step size $\Delta h = 0.1$, and $Re \in [2,000, 5,000]$, with a step size $\Delta Re = 100$ for various wave modes (see Table 1 in the work of Sorensen et al. [11]).

The different regimes can have a significant effect on the performance of the system, and there is a considerable body of work in the literature examining various methods of controlling the flow, e.g. via the insertion of a rod along the cylinder axis [12,13], a small rotating disk at the stationary wall [14], the use of magnetohydrodynamics [15,16], the addition of a second fluid with a slightly different density [17], and the application of a temperature gradient in the axial direction [9,18-23]. The latter case is of particular interest, as temperature gradients are a feature of many systems involving vortex breakdown,

such as the effect of temperature non-uniformity in tornadoes [19], combustion in vortex burners [24,25], and separation of compressed gases in Ranque-Hilsch vortex tubes [26,27], to name a few.

When a temperature difference across the cylinder axis, ΔT^* , exists, two additional non-dimensional groups are required to characterize the system; the Prandtl number, $Pr = \nu/\alpha$, and the Richardson number, $Ri = \beta \Delta T^* g/R\omega^2$, which represents the ratio of buoyancy to centrifugal forces. In the case of a non-isothermal swirling flow, an additional parameter of interest is the heat flow across the top/bottom plates, which is non-dimensionalized as the Nusselt number, $Nu = q''/k\Delta T^*/R$, where q'' is the heat flux at the upper plate and k is the thermal conductivity. In order to maintain $Nu = 1$ for the case of pure conduction, as is common in heat transfer analysis, the Nusselt number must be defined using the cylinder height as the characteristic length scale, $Nu^* = Nu.h$.

Depending on the sign of ΔT^* , the temperature gradients can act to stabilize the flow or promote vortex breakdown [9,18,19,21,28,29]. When the temperature gradient is positive (i.e. the top plate of the cylinder is hotter than the bottom plate), the critical Reynolds number for vortex-breakdown is reduced [18,30]. A similar effect is observed when a dense fluid is added to the bottom of the cylinder [17]. The positive thermal gradient can also lead to a dramatic change in the nature of vortex breakdown, with the appearance of a “two-cell” flow pattern, in which two counter-rotating toroidal vortices form in the top and bottom of the cylinder [18,21,23]. This layering results in a significant reduction in the Nusselt number [23]. However, it remains unclear what effect this layering may have on the torque transmitted through the fluid, which is a key factor in the performance of such rotating systems. Likewise, it is not known how further increases to the Richardson number may affect the development of the flow and the overall performance of the system when vortex breakdown has been already suppressed and layering is present.

This paper aims to address these questions and characterize the role of a temperature gradient on the flow dynamics in a variety of axisymmetric vortex breakdown regimes, as determined by Re and h . The problem is addressed using the Generalized Integral Transform Technique (GITT), which is a hybrid numerical-analytical methodology [31] that has previously been applied to fluid flow and heat transfer governed by the Navier-Stokes and energy equations [32-40], including cylindrical cavities [37-40]; however, a solution to the mixed convection problem in such geometry has not been implemented hitherto. Mathematical descriptions of the problem and the GITT methodology are outlined in the following section, the results are validated in Section 3.1 and are discussed in terms of flow, vorticity and temperature fields in Section 3.2; the effects of thermal gradients and induced flows on torque transmission, azimuthal velocity and heat transfer are discussed in Section 3.3, followed by some concluding remarks in Section 4.

2. Methodology

2.1. Mathematical formulation

A cylindrical container with an axial temperature difference imposed between the top and bottom plates is studied as shown in Fig 1. The flow in the container is assumed to be laminar, steady and incompressible, and the fluid is Newtonian with constant physical properties, with the exception of density, which depends on the temperature according to Boussinesq's approximation. Density changes result in both a centrifugal buoyancy force and a gravitational buoyancy force, which scale as $\sim \beta \Delta T^* \omega^2 R$ and $\sim \beta \Delta T^* g$, respectively. Therefore the ratio of gravitational to centrifugal buoyancy forces scales as $g/\omega^2 R$ (i.e. the inverse of the Froude number, Fr), which were in the range 3.7 – 15.4 for all the data presented in this paper, i.e. the centrifugal buoyancy forces were small compared to those due to gravity. For this reason, the centrifugal buoyancy terms are neglected in the analysis. Similarly, viscous dissipation and radiative heat transfer are expected to be negligible and are also disregarded.

The bottom plate rotates in the clockwise direction, i.e. as $\omega_b = -\omega$, while the top plate is stationary. The top plate is hotter than the bottom plate (with a temperature difference of ΔT^*), i.e. the flow is convectively stable. The cylinder wall is stationary and assumed to be adiabatic. The 2D governing equations for this problem are expressed in dimensionless form as follows:

$$\frac{1}{r} \frac{\partial(rv_r)}{\partial r} + \frac{\partial v_z}{\partial z} = 0 \quad (1)$$

$$v_r \frac{\partial v_r}{\partial r} - \frac{v_\theta^2}{r} + v_z \frac{\partial v_r}{\partial z} = -\frac{\partial P}{\partial r} + \frac{1}{\text{Re}} \left(\frac{\partial^2 v_r}{\partial r^2} + \frac{1}{r} \frac{\partial v_r}{\partial r} - \frac{v_r}{r^2} + \frac{\partial^2 v_r}{\partial z^2} \right) \quad (2)$$

$$v_r \frac{\partial v_z}{\partial r} + v_z \frac{\partial v_z}{\partial z} = -\frac{\partial P}{\partial z} + \frac{1}{\text{Re}} \left(\frac{\partial^2 v_z}{\partial r^2} + \frac{1}{r} \frac{\partial v_z}{\partial r} + \frac{\partial^2 v_z}{\partial z^2} \right) + \text{RiT} \quad (3)$$

$$v_r \frac{\partial v_\theta}{\partial r} + \frac{v_r v_\theta}{r} + v_z \frac{\partial v_\theta}{\partial z} = \frac{1}{\text{Re}} \left(\frac{\partial^2 v_\theta}{\partial r^2} + \frac{1}{r} \frac{\partial v_\theta}{\partial r} - \frac{v_\theta}{r^2} + \frac{\partial^2 v_\theta}{\partial z^2} \right) \quad (4)$$

$$v_r \frac{\partial T}{\partial r} + v_z \frac{\partial T}{\partial z} = \frac{1}{\text{RePr}} \left(\frac{\partial^2 T}{\partial r^2} + \frac{1}{r} \frac{\partial T}{\partial r} + \frac{\partial^2 T}{\partial z^2} \right) \quad (5)$$

The following flow and temperature boundary conditions are specified in non-dimensional form:

$$v_r(0,z) = 0, \quad \frac{\partial v_z(0,z)}{\partial r} = 0, \quad v_\theta(0,z) = 0, \quad \frac{\partial T(0,z)}{\partial r} = 0 \quad (6)$$

$$v_r(1,z) = 0, \quad v_z(1,z) = 0, \quad v_\theta(1,z) = 0, \quad \frac{\partial T(1,z)}{\partial r} = 0 \quad (7)$$

$$v_r(r,0) = 0, \quad v_z(r,0) = 0, \quad v_\theta(r,0) = -r, \quad T(r,0) = -\frac{1}{2} \quad (8)$$

$$v_r(r,h) = 0, \quad v_z(r,h) = 0, \quad v_\theta(r,h) = 0, \quad T(r,h) = \frac{1}{2} \quad (9)$$

Equations (1) to (9) are normalized as follows:

$$r = \frac{r^*}{R}, \quad z = \frac{z^*}{R}, \quad v_r = \frac{v_r^*}{R\omega}, \quad v_z = \frac{v_z^*}{R\omega}, \quad v_\theta = \frac{v_\theta^*}{R\omega}, \quad P = \frac{P^*}{\rho R^2 \omega^2}, \quad T = \frac{T^* - T_0}{\Delta T^*} \quad (10)$$

In order to implement the GITT approach to solve the above equations, a streamfunction formulation is employed [32-40]. The two-dimensional streamfunction is defined in terms of the velocity components in the r and z directions, respectively, as:

$$v_r = \frac{1}{r} \frac{\partial \psi}{\partial z}, \quad v_z = -\frac{1}{r} \frac{\partial \psi}{\partial r} \quad (11)$$

and the mathematical formulation of this problem in terms of streamfunction can be written as:

$$\frac{1}{r} \frac{\partial \psi}{\partial z} \frac{\partial (E^2 \psi)}{\partial r} - \frac{1}{r} \frac{\partial \psi}{\partial r} \frac{\partial (E^2 \psi)}{\partial z} - \frac{2}{r^2} \frac{\partial \psi}{\partial z} E^2 \psi - 2v_\theta \frac{\partial v_\theta}{\partial z} = \frac{1}{\text{Re}} E^4 \psi - \text{Ri} \frac{\partial T}{\partial r} \quad (12)$$

$$\frac{1}{r} \frac{\partial \psi}{\partial z} \left(\frac{\partial v_\theta}{\partial r} + \frac{v_\theta}{r} \right) - \frac{1}{r} \frac{\partial \psi}{\partial r} \frac{\partial v_\theta}{\partial z} = \frac{1}{\text{Re}} \left(\frac{\partial^2 v_\theta}{\partial r^2} + \frac{1}{r} \frac{\partial v_\theta}{\partial r} - \frac{v_\theta}{r^2} + \frac{\partial^2 v_\theta}{\partial z^2} \right) \quad (13)$$

$$\frac{1}{r} \frac{\partial \psi}{\partial z} \frac{\partial T}{\partial r} - \frac{1}{r} \frac{\partial \psi}{\partial r} \frac{\partial T}{\partial z} = \frac{1}{\text{Re Pr}} \nabla^2 T \quad (14)$$

$$\lim_{r \rightarrow 0} \left[\frac{\psi(r,z)}{r} \right] = 0, \quad \lim_{r \rightarrow 0} \left\{ \frac{\partial}{\partial r} \left[\frac{1}{r} \frac{\partial \psi(r,z)}{\partial r} \right] \right\} = 0, \quad v_\theta(0,z) = 0, \quad \frac{\partial T(0,z)}{\partial r} = 0 \quad (15)$$

$$\psi(1,z) = 0, \quad \frac{\partial \psi(1,z)}{\partial r} = 0, \quad v_\theta(1,z) = 0, \quad \frac{\partial T(1,z)}{\partial r} = 0 \quad (16)$$

$$\psi(r,0) = 0, \quad \frac{\partial \psi(r,0)}{\partial z} = 0, \quad v_\theta(r,0) = -r, \quad T(r,0) = -\frac{1}{2} \quad (17)$$

$$\psi(r,h) = 0, \quad \frac{\partial \psi(r,h)}{\partial z} = 0, \quad v_\theta(r,h) = 0, \quad T(r,h) = \frac{1}{2} \quad (18)$$

with the associated operators E^2 , E^4 and ∇^2 defined as:

$$E^2 = \frac{\partial^2}{\partial r^2} - \frac{1}{r} \frac{\partial}{\partial r} + \frac{\partial^2}{\partial z^2},$$

$$E^4 = E^2(E^2) = \frac{\partial^4}{\partial r^4} - \frac{2}{r} \frac{\partial^3}{\partial r^3} + \frac{3}{r^2} \frac{\partial^2}{\partial r^2} - \frac{3}{r^3} \frac{\partial}{\partial r} - \frac{2}{r} \frac{\partial^3}{\partial r \partial z^2} + 2 \frac{\partial^4}{\partial r^2 \partial z^2} + \frac{\partial^4}{\partial z^4}, \quad (19)$$

$$\nabla^2 = \frac{\partial^2}{\partial r^2} + \frac{1}{r} \frac{\partial}{\partial r} + \frac{\partial^2}{\partial z^2}$$

2.2. Solution methodology

The streamfunction formulation of the problem above, Eqs. (12) to (18), is solved by means of appropriate eigenfunction expansions. The details of the GITT approach are given as follows, as an extension to hybrid solutions previously implemented [31-40]. The GITT approach [31-40] is now applied in the solution of Eqs. (12) to (18), following previous developments on the hybrid integral transforms solution of the Navier-Stokes and energy equations in cylindrical coordinates [37-40]. Therefore, the respective eigenfunctions, eigenvalues, norms and orthogonality properties for each potential in the present problem are as follows:

Streamfunction:

$$\frac{d^4 X_i(r)}{dr^4} - \frac{2}{r} \frac{d^3 X_i(r)}{dr^3} + \frac{3}{r^2} \frac{d^2 X_i(r)}{dr^2} - \frac{3}{r^3} \frac{dX_i(r)}{dr} = -\gamma_i^2 \left[\frac{d^2 X_i(r)}{dr^2} - \frac{1}{r} \frac{dX_i(r)}{dr} \right] \quad (20)$$

$$\lim_{r \rightarrow 0} \left[\frac{X_i(r)}{r} \right] = 0, \quad \lim_{r \rightarrow 0} \left\{ \frac{d}{dr} \left[\frac{1}{r} \frac{dX_i(r)}{dr} \right] \right\} = 0 \quad (21)$$

$$X_i(1) = 0, \quad \frac{dX_i(1)}{dr} = 0 \quad (22)$$

The general solution of the problem given by Eqs. (20) to (22) and the transcendental equation to compute the eigenvalues γ_i 's are expressed as:

$$X_i(r) = r^2 - \frac{rJ_1(\gamma_i r)}{J_1(\gamma_i)}, \quad J_2(\gamma_i) = 0, \quad \text{for } i=1,2,3,\dots \quad (23)$$

The eigenfunctions satisfy the following orthogonality property:

$$\int_0^1 \frac{1}{r} \frac{dX_i(r)}{dr} \frac{dX_j(r)}{dr} dr = \begin{cases} 0, & i \neq j \\ L_i, & i = j \end{cases}, \quad L_i = \int_0^1 \frac{1}{r} \left[\frac{dX_i(r)}{dr} \right]^2 dr = \frac{\gamma_i^2}{2} \quad (24)$$

Azimuthal velocity:

$$\frac{1}{r} \frac{d}{dr} \left[r \frac{dY_i(r)}{dr} \right] - \left(\frac{1}{r^2} - \lambda_i^2 \right) Y_i(r) = 0 \quad (25)$$

$$Y_i(0) = 0, \quad Y_i(1) = 0 \quad (26)$$

The eigenquantities are expressed as:

$$Y_i(r) = J_1(\lambda_i r), \quad J_1(\lambda_i) = 0, \quad \text{for } i=1,2,3,\dots \quad (27)$$

$$\int_0^1 r Y_i(r) Y_j(r) dr = \begin{cases} 0, & i \neq j \\ M_i, & i = j \end{cases}, \quad M_i = \int_0^1 r Y_i^2(r) dr = \frac{J_0^2(\lambda_i)}{2} \quad (28)$$

Temperature:

$$\frac{1}{r} \frac{d}{dr} \left[r \frac{d\Gamma_i(r)}{dr} \right] + \mu_i^2 \Gamma_i(r) = 0 \quad (29)$$

$$\frac{d\Gamma_i(0)}{dr} = 0, \quad \frac{d\Gamma_i(1)}{dr} = 0 \quad (30)$$

Similarly, the eigenquantities are expressed as:

$$\Gamma_i(r) = J_0(\mu_i r), \quad J_1(\mu_i) = 0, \quad \text{for } i=1,2,3,\dots \quad (31)$$

$$\int_0^1 r \Gamma_i(r) \Gamma_j(r) dr = \begin{cases} 0, & i \neq j \\ N_i, & i = j \end{cases}, \quad N_i = \int_0^1 r \Gamma_i^2(r) dr = \frac{J_0^2(\mu_i)}{2} \quad (32)$$

Once the eigenvalue problem is fully defined the next step in the methodology is to determine integral transform pairs which will allow integral transformation of the partial differential equations in the streamfunction formulation of the problem. Therefore, the eigenvalue problems given by Eqs. (20) to (32) allow the following definitions:

$$\bar{\Psi}_i(z) = -\frac{1}{L_i} \int_0^1 \frac{d}{dr} \left[\frac{1}{r} \frac{dX_i(r)}{dr} \right] \Psi(r,z) dr, \quad \text{transform} \quad (33)$$

$$\Psi(r,z) = \sum_{i=1}^{\infty} X_i(r) \bar{\Psi}_i(z), \quad \text{inverse} \quad (34)$$

$$\bar{v}_{\theta,i}(z) = \frac{1}{M_i} \int_0^1 r Y_i(r) v_{\theta}(r,z) dr, \quad \text{transform} \quad (35)$$

$$v_{\theta}(r,z) = \sum_{i=1}^{\infty} Y_i(r) \bar{v}_{\theta,i}(z), \quad \text{inverse} \quad (36)$$

$$\bar{T}_i(z) = \frac{1}{N_i} \int_0^1 r \Gamma_i(r) T(r,z) dr, \quad \text{transform} \quad (37)$$

$$T(r,z) = \sum_{i=1}^{\infty} \Gamma_i(r) \bar{T}_i(z), \quad \text{inverse} \quad (38)$$

The integral transformation of the problem is performed by multiplying the partial differential equations, Eqs. (12), (13) and (14), together with the boundary conditions, Eqs. (17) and (18), by $X_i(r)/r$, $rY_i(r)$, and $r\Gamma_i(r)$, respectively, and then integrating over the domain $[0,1]$ in the radial direction. The inverse formulae given by Eqs. (34), (36), and (38) are employed for the streamfunction, azimuthal velocity and temperature potentials, respectively. After some algebraic manipulations, the following system of coupled nonlinear ordinary differential equations (ODEs) for determining the transformed potentials, $\bar{\Psi}_i(z)$, $\bar{v}_{\theta,i}(z)$, and $\bar{T}_i(z)$, corresponding to the transformed streamfunction, azimuthal velocity component and temperature, respectively, is then obtained:

$$\sum_{j=1}^{\infty} A_{ij} \frac{d^4 \bar{\psi}_j(z)}{dz^4} = -\frac{\gamma_i^4}{2} \bar{\psi}_i(z) + \gamma_i^2 \frac{d^2 \bar{\psi}_i(z)}{dz^2} + \text{Re} \left\{ \sum_{j=1}^{\infty} \sum_{k=1}^{\infty} \left[B_{ijk} \bar{\psi}_j(z) \frac{d\bar{\psi}_k(z)}{dz} + C_{ijk} \frac{d\bar{\psi}_j(z)}{dz} \frac{d^2 \bar{\psi}_k(z)}{dz^2} + D_{ijk} \bar{\psi}_j(z) \frac{d^3 \bar{\psi}_k(z)}{dz^3} \right] + \sum_{j=1}^{\infty} \sum_{k=1}^{\infty} E_{ijk} \bar{v}_{\theta,j}(z) \frac{d\bar{v}_{\theta,k}(z)}{dz} + \text{Re} \sum_{j=1}^{\infty} F_{ij} \bar{T}_j(z) \right\} \quad (39)$$

$$\frac{d^2 \bar{v}_{\theta,i}(z)}{dz^2} = \lambda_i^2 \bar{v}_{\theta,i}(z) + \text{Re} \sum_{j=1}^{\infty} \sum_{k=1}^{\infty} \left[G_{ijk} \bar{v}_{\theta,j}(z) \frac{d\bar{\psi}_k(z)}{dz} + H_{ijk} \frac{d\bar{v}_{\theta,j}(z)}{dz} \bar{\psi}_k(z) \right] \quad (40)$$

$$\frac{d^2 \bar{T}_i(z)}{dz^2} = \mu_i^2 \bar{T}_i(z) + \text{Re} \text{Pr} \sum_{j=1}^{\infty} \sum_{k=1}^{\infty} \left[I_{ijk} \bar{T}_j(z) \frac{d\bar{\psi}_k(z)}{dz} + J_{ijk} \frac{d\bar{T}_j(z)}{dz} \bar{\psi}_k(z) \right] \quad (41)$$

$$\bar{\psi}_i(0) = 0, \quad \frac{d\bar{\psi}_i(0)}{dz} = 0, \quad \bar{v}_{\theta,i}(0) = -\bar{f}_i, \quad \bar{T}_i(0) = -\frac{\bar{g}_i}{2} \quad (42)$$

$$\bar{\psi}_i(h) = 0, \quad \frac{d\bar{\psi}_i(h)}{dz} = 0, \quad \bar{v}_{\theta,i}(h) = 0, \quad \bar{T}_i(h) = \frac{\bar{g}_i}{2} \quad (43)$$

where the various coefficients are given by:

$$A_{ij} = \int_0^1 \frac{X_i(r) X_j(r)}{r} dr, \quad B_{ijk} = \int_0^1 X_i(r) \left\{ \left[\frac{X_j'''(r)}{r^2} - \frac{3X_j''(r)}{r^3} + \frac{3X_j'(r)}{r^4} \right] X_k(r) - \frac{X_j'(r) X_k''(r)}{r^2} + \frac{X_j'(r) X_k'(r)}{r^3} \right\} dr \quad (44)$$

$$C_{ijk} = \int_0^1 X_i(r) X_j(r) \left[\frac{X_k'(r)}{r^2} - \frac{2X_k(r)}{r^3} \right] dr, \quad D_{ijk} = -\int_0^1 \frac{X_i(r) X_j'(r) X_k(r)}{r^2} dr \quad (45)$$

$$E_{ijk} = -2 \int_0^1 \frac{X_i(r) Y_j(r) Y_k(r)}{r} dr, \quad F_{ij} = \int_0^1 X_i(r) \Gamma_j'(r) dr \quad (46)$$

$$G_{ijk} = \frac{1}{M_i} \int_0^1 Y_i(r) \left[Y_j'(r) + \frac{Y_j(r)}{r} \right] X_k(r) dr, \quad H_{ijk} = -\frac{1}{M_i} \int_0^1 Y_i(r) Y_j(r) X_k'(r) dr \quad (47)$$

$$I_{ijk} = \frac{1}{N_i} \int_0^1 \Gamma_i(r) \Gamma_j'(r) X_k(r) dr, \quad J_{ijk} = -\frac{1}{N_i} \int_0^1 \Gamma_i(r) \Gamma_j(r) X_k'(r) dr \quad (48)$$

$$\bar{f}_i = \frac{1}{M_i} \int_0^1 r^2 Y_i(r) dr, \quad \bar{g}_i = \frac{1}{N_i} \int_0^1 r \Gamma_i(r) dr \quad (49)$$

Once the transformed potentials are obtained, the inverse formulae are employed to derive the streamfunction, the azimuthal velocity component and temperature (Eqs. (34), (36), and (38)). For example, using the definition of the streamfunction (Eq. (11)) and the inverse transform, the axial and radial velocities can be expressed in terms of the transformed streamfunction, as follows:

$$v_r(r, z) = \sum_{i=1}^{\infty} \frac{X_i(r)}{r} \frac{d\bar{\psi}_i(z)}{dz}, \quad v_z(r, z) = -\sum_{i=1}^{\infty} \frac{1}{r} \frac{dX_i(r)}{dr} \bar{\psi}_i(z) \quad (50)$$

A similar approach is followed to estimate other parameters of interest in this study such as the torque coefficient, the vorticity and the Nusselt number. Thus, the torque coefficient is defined as:

$$C_T = 2 \int_0^1 r^2 \frac{\partial v_\theta}{\partial z} \Big|_{z=0} dr \quad (51)$$

and by introducing the inverse formula, Eq. (36), for the v_θ velocity component into the definition, it can be expressed as:

$$C_T = \sum_{i=1}^{\infty} \bar{h}_i \frac{d\bar{v}_{\theta,i}(0)}{dz}, \quad \bar{h}_i = 2 \int_0^1 r^2 Y_i(r) dr \quad (52)$$

The azimuthal vorticity component is computed from its definition:

$$\omega_\theta = \frac{\partial v_r}{\partial z} - \frac{\partial v_z}{\partial r} = \frac{1}{r} \frac{\partial^2 \psi}{\partial z^2} + \frac{1}{r} \frac{\partial^2 \psi}{\partial r^2} - \frac{1}{r^2} \frac{\partial \psi}{\partial r} \quad (53)$$

and by introducing the inverse formula given by Eq. (34) it becomes:

$$\omega_\theta = \sum_{i=1}^{\infty} \left[\frac{X_i(r)}{r} \frac{d^2 \bar{\psi}_i(z)}{dz^2} + \frac{1}{r} \frac{d^2 X_i(r)}{dr^2} \bar{\psi}_i(z) - \frac{1}{r^2} \frac{dX_i(r)}{dr} \bar{\psi}_i(z) \right] \quad (54)$$

Finally, the local Nusselt numbers at the two lids are defined as

$$Nu_0(r) = \frac{\partial T}{\partial z} \Big|_{z=0}, \quad Nu_h(r) = \frac{\partial T}{\partial z} \Big|_{z=h} \quad (55)$$

and by making use of the inverse formula given by Eq. (38) they are expressed as follows:

$$Nu_0(r) = \sum_{i=1}^{\infty} \Gamma_i(r) \frac{d\bar{T}_i(0)}{dz}, \quad Nu_h(r) = \sum_{i=1}^{\infty} \Gamma_i(r) \frac{d\bar{T}_i(h)}{dz} \quad (56)$$

The average Nusselt number is obtained by integrating the local Nusselt number either on the bottom or the top lid, thus

$$\bar{Nu}_i = 2 \int_0^1 r Nu_i(r) dr, \quad i=0 \text{ or } h \quad (57)$$

Once the streamfunction and angular velocity component fields have been determined from the solution of Eqs. (12) to (18), the relations of the radial and axial velocity components in terms of the streamfunction, Eqs. (11), can be recalled in terms of the inverse formula, Eq. (34), as given by Eqs. (50). Then, either through Eq. (2) or Eq. (3), the pressure field can be determined by substituting the relations for the three velocity components. In fact, since the analytical eigenfunction expansion is

proposed in the radial direction, it is more appropriate to employ Eq. (2) in determining the pressure field, since an analytical integration in the radial direction can be achieved exactly.

A computational code in Fortran 2003 was developed and implemented to solve the coupled system of ODEs given by Eqs. (39) to (43) making use of the DBVPFD subroutine from the IMSL Library [41]. The system is truncated to a sufficiently large number of terms (NF for the streamfunction, NV for the azimuthal velocity, and NT for the temperature), in order to reach a prescribed overall relative error in obtaining the original potentials. The characteristic of this subroutine is that it solves a (parameterized) system of ordinary differential equations with boundary conditions at two-points using a variable order, variable step-size finite difference method with deferred corrections. It also provides the important feature of automatically controlling the relative error in the solution of the system of ODEs, thus allowing the user to establish error targets for the transformed potentials.

A relative error target of 10^{-4} , which represents four significant digits for the transformed potentials, was prescribed in this study. A careful analysis of the convergence behavior of the results revealed that a number of terms in the expansions of $N=NF=NV=NT=90$ was sufficient to guarantee at least three converged significant digits for the velocity and temperature fields. In this hybrid integral transform method, the only numerical task is to solve the system of coupled ordinary differential equations. In the present work, as mentioned before, we have used the subroutine DBVPFD from the IMSL Library [41]. The number of points in the mesh is a function of the governing parameters, mainly the Reynolds number. The mesh size is in fact not imposed, but is achieved to satisfy the adaptive error control, from the user prescribed relative error. A summary of the grid sizes achieved in the present work is shown in Table 1.

We focus on three combinations of Reynolds number and aspect ratio; $Re = 1492$, $h = 1.5$ in Section 3.2.1; $Re = 2126$, $h = 2.5$ in Section 3.2.2; and $Re = 3061$, $h=3.5$ in Section 3.2.3. These parameters are chosen to match previous experimental work by Escudier [6], who showed that they corresponded to different regimes of vortex breakdown, with one, two and three recirculation bubbles, respectively. In each case, Escudier showed that the flow was laminar, 2D and axisymmetric, which is consistent with our formulation (Section 2). It should be noted that in the h - Re regime map calculated by Sorensen et al. [11], our highest Reynolds number case lies just above the regime boundary for unsteady flow, which cannot be captured by our model. However, we note that our results are consistent with the observations of Escudier [6] (as will be discussed in Section 3.1), and that as the Richardson number is increased, the thermal gradient and associated layering of the fluid are expected to oppose the onset of three-dimensionality and unsteady behavior.

In all cases, the Prandtl number was fixed at $Pr=1$. At this point, it is important to mention that taking $Pr=1$, and considering the employed combinations of dimensionless parameters, $Re=1492$, 2126, and 3061, $h=1.5$, 2.5, and 3.5 and $Ri=0$, 0.01, and 0.1, the largest value for the Grashof number is about 0.937×10^7 , which corresponds to the largest values of Re ($=3061$) and Ri ($=0.1$). Considering the kinematic viscosity and expansion coefficient of air at $T^*=25^\circ\text{C}$, for instance, the temperature difference

between the lids can be computed as a function of the cylinder radius, being 55.6°C, 6.96°C and 0.87°C, for radii of 5, 10 and 20 cm, respectively, illustrating the importance of the cylinder geometry in inducing the mixed convection effects.

3. Results

3.1. Validation and verification of the technique

In order to confirm the ability of our approach to accurately capture the physics of the problem, results obtained for three cases, representing different forms of steady state vortex breakdown (VB) are compared to flow visualization experiments of Escudier [6]. These are: single bubble VB case, $Re = 1492$, $h = 1.5$ (Fig. 2(a)); double bubble VB case, $Re = 2126$, $h = 2.5$ (Fig. 2(b)); and triple bubble VB case, $Re = 3061$, $h = 3.5$ (Fig. 2(c)). The Richardson number is zero in all cases, indicating the absence of buoyancy forces. It can be seen that the GITT methodology implemented in this study is capable of reproducing not just the number of breakdown bubbles present in the flow, but also their length and axial location of the bubbles within the flow.

The present GITT results were further validated by comparing the average Nusselt numbers against numerically computed ones from the work of Omi and Iwatsu [21], that used a finite-difference scheme for the same mixed convection problem analyzed herein. Figure 3 shows the variation of Nusselt number as a function of the Richardson number for the case of $Re = 1000$ and $h = 2$; good agreement between the present results and those in [21] can be observed providing confidence that the GITT technique can be fully utilized to further explore the physics of non-isothermal flows in the same systems.

In the following sections, the effect of temperature gradients on the flow are explored for each of these three cases.

3.2. VB suppression and buoyancy induced flow transitions

3.2.1. Single VB case ($Re = 1492$, $h = 1.5$)

The effects of thermal gradients on the simplest case of vortex breakdown – a single, axisymmetric bubble – are shown in Fig. 4 for $Re = 1492$, $h = 1.5$ and four cases of $Ri = 0, 0.01, 0.02$ and 0.1 . The $Ri = 0$ case (base flow) corresponds to a complete decoupling of the velocity and temperature fields, in which no natural convection takes place. In the absence of any rotation of the bottom plate (i.e. for $Re = 0$), the temperature field would vary linearly from the top to the bottom with horizontal isotherms and the velocity field would be zero, as a pure heat conduction problem. However, in Fig. 4(a) the rotation of the bottom plate imparts angular velocity and a centrifugal force to the fluid near $z = 0$, and this force pushes the fluid radially outward. As the fluid reaches the cylinder walls it is

diverted upward, producing jets near $|r| \gtrsim 0.75$, with a broad return flow in the central region of the cylinder. The upward jets and the return flow result in the characteristic flow structure of centrifugal systems, with an axial vortex core aligned along the cylinder axis. This undergoes a breakdown, with a single bubble present at $z = 1$.

The downward flow in the center of the cylinder drags down hot fluid, as can be seen in the temperature field in Fig. 4(a,ii). This occurs in the absence of buoyancy forces ($Ri = 0$); however, when $Ri > 0$, the buoyancy forces act to *oppose* the return flow (and likewise to suppress the upward jets near the cylinder walls). This effect can be seen in Figs. 4(b) and 4(c), where there is a weakening of the magnitude of the streamfunction both in the jets and near the central axis. The buoyancy force also causes the isotherms near the top plate to become more horizontal, as the weaker return flow near the cylinder axis drags less fluid downward. This weakening of the downward flow also reduces the size of the vortex breakdown bubble at $Ri = 0.01$ and, by $Ri = 0.02$, VB is completely suppressed.

When the relative effects of free convection are increased further ($Ri = 0.1$, Fig. 4(d)), the buoyancy forces acting on the hot fluid near the top of the domain are so strong that the inertia forces arising from the motion of the bottom plate cannot drag the fluid downward and the flow is divided into a “two cells” structure. Below $z \approx 1.25$, the streamfunction, temperature and vorticity fields are similar to those for the “single cell” cases (Figs. 4(a-c)), except that they appear compressed vertically into the region $z < 1.25$. Above this point, a counter-rotating toroidal vortex exists, which has a much smaller magnitude than the flow that occurs below (Fig. 4(d,iii)). Within this upper layer ($z \gtrsim 1.25$), the isotherms are close to horizontal, indicating the dominance of conduction over convection.

The azimuthal vorticity fields (bottom row of Fig. 4) for all three cases examined are dominated by the high magnitude (negative) vorticity near the bottom plate (which also has a negative rotation speed, $\omega_b < 0$) and two “arms” near the cylinder walls which correspond to the upward jets, which also have a negative radial velocity due to their recent presence at the rotating bottom plate. In Fig. 4(a,iii), two lobes of positive vorticity can be seen near the location of the vortex bubble at $z \approx 1$; as Ri is increased and the vortex breakdown is suppressed, these lobes are weakened and are shifted downward (Figs. 4(b,iii) and 4(c,iii)). As the Richardson number is increased and the return flow is suppressed, the magnitude of the vorticity at the upper plate is reduced, which implies a reduction in the magnitude of the stresses and torque acting on this surface. The effect of Ri on the torque coefficient will be discussed in detail in Section 3.3.

In order to explore the transition from a single layer to a double layer flow structure near $Ri = 0.1$ and to investigate whether further transitions occur, an additional series of simulations were performed spanning the range $Ri = 0.03 - 1$, which are summarized in Fig. 5. As the Richardson number is increased from $Ri = 0.02$ to 0.03 (Figs. 5(b) and 5(c)), the buoyancy forces acting on the hot fluid near the upper surface cause a small toroidal region of counter-flow to form, which in the rz -plane manifests as two lobes centered at $|r| \approx 0.3$ in Fig. 5(c). This region grows in size as the Richardson number is increased further, until it occupies the entire upper part of the cylinder ($Ri = 0.1$, Fig. 5(d)).

Interestingly, a further increase in Ri to 0.15 (Fig. 5(e)) causes a new region of flow to form at the upper plate by the cylinder walls ($|r| \gtrsim 0.5$), which has an opposite rotation direction (in the meridian plane) to that of the counter flow regions that appeared for $Ri = 0.03$ and 0.1 (and the same rotational direction as the flow in the lower half of the cylinder). By $Ri = 0.2$ (Fig. 5(f)), this new region of counter flow has grown to occupy the entire flow domain near the top plate (i.e. for $z \gtrsim 1.3$), leading to a three-layer flow structure. Further increases in Ri (Figs. 5(g) and 5(h)) lead to the formation of additional regions of counter flow and additional fluid layers.

3.2.2. Double VB case ($Re = 2126$, $h = 2.5$)

In Fig. 6 the effect of Richardson number is explored for a case in which a two-bubble vortex breakdown occurs. The two bubbles can clearly be seen in Fig. 6(a), centered along the cylinder axis at $z \approx 1.1$ and 1.85. As in the single breakdown case ($Re = 1492$, $h = 1.5$), two strong upward jets are visible near the cylinder walls. A small increase in the Richardson number to $Ri = 0.005$ (Fig. 6(b)) causes the vortex breakdown bubbles to shrink and elongate, and by $Ri = 0.01$ (Fig. 6(c)) they have merged to form a single long bubble. In the colorful terminology of Lugt and Abboud [9], an ‘onion’ bubble and an ‘egg’ bubble ($Ri = 0$) have transitioned to two ‘egg’ bubbles ($Ri = 0.005$) and finally merged to form a ‘cucumber’ bubble ($Ri = 0.01$).

When the Richardson number is increased to $Ri = 0.015$ (Fig. 6(d)), the buoyancy forces cause small regions of counter flow to form at the upper plate (as was seen for $Re = 1492$, $Ri = 0.03$ in Fig. 5(c)); however, in this case these regions have merged with the nearby vortex breakdown bubble. As in the previous case, further increases in Ri cause this new fluid region to occupy the entire upper plate and the transition to a multi-layered flow pattern ($Ri = 0.05$, Fig. 6(e)). Increasing the Richardson number further leads to the formation of additional layers (Figs. 6(f-j)), although not all of the newly formed layers extend all the way from the cylinder walls to the central axis. At high Richardson number ($Ri = 1$, Fig. 6(j)), the various regions of counter flow at the upper half of the cylindrical container become indistinct, and the flow appears to revert to a structure with less layers.

3.2.3. Triple VB case ($Re = 3061$, $h = 3.5$)

Finally, we analyze the effects of buoyancy forces for a case of vortex breakdown with three bubbles at $Re = 3061$, $h = 3.5$ (Fig. 7). In the absence of any buoyancy forces (Fig. 7(a)), three bubbles are present at $z \approx 1.4$, 2 and 2.8, with the lower two vortices very close to each other. At a very low Richardson number ($Ri = 0.001$, Fig. 7(b)), these vortices merge, with the third bubble at $z \approx 2.8$ weakened slightly. By $Ri = 0.005$ (Fig. 7(c)) all three bubbles have merged into a single one. Similar to what was observed in the previous section, a further increase in Ri causes the growth of regions of counter rotating flow at the upper plate ($Ri = 0.007$, Fig. 7(d)) which merge with the vortex breakdown

bubble ($Ri = 0.03$, Fig. 7(e)), leading to the formation of new fluid layers. Ultimately as Richardson number is increased to $Ri = 1$, these layers begin to merge with each other as in the case of the two bubbles.

Figure 8 summarizes the change in the number of fluid layers for the three cases discussed above. The number of layers was evaluated by identifying the recirculation zones occupying a specific portion of the cavity flow. In all cases, at $Ri = 0$, the flow is characterized by a single flow cell (one layer) which increases smoothly as Ri is increased. A very weak effect of buoyancy ($Ri < 0.4$) is sufficient to induce a multi-layered flow pattern. The number of layers seems to be dependent on the type of VB in this Ri range. However, overall Ri has a non-monotonic effect on flow structure, with an increase in Richardson number above approximately 0.3 leading to a slight reduction in number of layers formed, as the latter start to become indistinct.

It is clear that for the limiting case of $Ri/Re \rightarrow 0$, the flow will be entirely stable and will therefore contain a single layer (in this case of stagnant fluid), as occurs for $Ri = 0$. Therefore, further increases in the Richardson number beyond $Ri = 1$, when Re is held constant, can be expected to lead to a gradual reduction in the number of layering.

3.3. Effect of flow structure on torque, azimuthal velocity and heat transport

Two key parameters in the performance of the system are the torque acting on the upper plate and the heat flux through this plate, which are expressed in terms of the torque coefficient, Eq. (52), and the average Nusselt number, Eq. (57), respectively. The variation in the torque coefficient with Ri for each of the three cases is shown in Fig. 9(a). Although the absolute values of C_T depend on both Re and h , in all three cases C_T declines smoothly with Ri . The reduction in C_T with respect to the value at $Ri = 0$ can be described using the empirical equation

$$C_T - C_{T,Ri=0} = -1.52Ri^{0.583} \quad (58)$$

as indicated by the black line in Fig. 9(b). This relationship holds regardless of how many layers are present in the flow, indicating that these transitions have a very weak effect on the shear stresses acting on the upper plate. However, Eq. (58) does not provide information on how the rotating flow varies within the domain. In order to characterize this variation, the absolute value of the mean azimuthal velocity component, $v_{\theta,m} = 2 \int_0^1 rv_{\theta} dr$, is plotted as a function of axial location in Fig. 10 for the sample case of $Re = 3061$, $h = 3.5$ (which corresponds to the flow fields presented in Fig. 7). At low Richardson number ($Ri = 0$ and 0.005), the streamlines in Fig. 7(a) and 7(c) show that a triple and single vortex breakdown bubble are present; these bubbles do not appear to have a significant effect on the azimuthal velocity profiles in Fig. 10, which exhibit only small, barely noticeable variations at the points

where the bubbles occur. Apart from these small fluctuations, the profiles are steep at either plate ($z = 0$ and 3.5), and between these boundaries the profiles vary smoothly.

As the Richardson number is increased to 0.03 (Fig. 7(e)), the flow transitions to a layered state, with the layering occurring near $z = 2.8$. This point coincides with a sudden reduction in the mean azimuthal velocity (green line in Fig. 10). Likewise, for $Ri = 0.1$ and 1 , layering extends to depths of $z \approx 2$ and 1 (Fig. 7(g) and 7(j)), respectively, which correspond to clear inflection points in the corresponding angular velocity profiles in Fig. 10. This result indicates that in the absence of layering the mean azimuthal velocity varies smoothly throughout the vessel and is only weakly affected by vortex breakdown; however, the transition to a layered state has a very large effect, leading to an exponential decline with distance from the rotating plate. Fig. 10 suggests that in terms of the operation of rotating machinery in the presence of temperature gradients, the layering state is likely to have a significantly greater impact on performance compared to vortex breakdown.

The variation in the average Nusselt number with Richardson number is shown in Fig. 11 for all three cases. A positive Nusselt number indicates heat flowing *into* the fluid from the top plate. The $Ri = 0$ case here corresponds to completely decoupled temperature and velocity fields (rather than simply an isothermal case). As was discussed previously, increasing Ri causes the plate-driven convection to be opposed by the buoyancy forces, and the flow tends to develop a fluid layered structure. The point at which layering occurs coincides with a sharp reduction in \bar{Nu} , as the weak flow in the fluid layer near the upper plate acts as an insulating layer, restricting heat transfer. Figure 11 indicates that the critical Richardson number at which layering occurs and heat transfer is restricted increases with Re and h .

Our results indicate that Re and h play an important role in the heat flux through swirling flows in enclosed geometries and by controlling the presence or absence of fluid layering, the heat transfer performance can be optimized, depending on the requirements of the system.

4. Concluding remarks

The effect of thermal gradients on the vortex breakdown in the flow in a cylindrical container with a rotating bottom plate was examined using the GITT approach. The streamfunction formulation was employed and the problem was solved for imposed temperature differences acting in the opposite direction to the base flow. Different aspect ratios, Re and Ri numbers were examined in order to capture three cases of vortex breakdown (exhibiting a single, double and triple bubbles respectively) and explore the stabilizing effect of buoyancy forces.

The GITT approach was able to capture the different vortex breakdown phenomena reported in the literature for the isothermal case and allowed flow transitions to be explored for a wide range of Richardson numbers. In all three cases investigated, increasing the magnitude of the buoyancy forces

resulted in the suppression of vortex breakdown and at sufficiently high Richardson numbers, led to the onset of a layered fluid structure. The stratification was attributed to the opposing actions of the (destabilizing) centrifugal forces and the (stabilizing) buoyancy forces. In the case of double and triple breakdown, the suppression of vortex breakdown occurred through a gradual merging process and the emergence of a counter rotating flow near the top plate. The number of these counter rotating layers gradually increased with Ri and the layers occupied more of the fluid domain, until a critical Richardson number was reached, after which further increases in Ri lead to the merger of layers.

The impact of these flow transitions on the torque coefficient, mean angular velocity profiles and Nusselt number was examined. It was found that the change in the torque coefficient relative to the base (isothermal) case ($Ri = 0$) scales with Ri in a power law relationship, regardless of the Reynolds number, aspect ratio or the number of fluid layers present. Outside the stratified region of the flow and the vicinity of the solid walls, the mean angular velocity varies smoothly between bottom and upper plate and is only weakly affected by the presence of vortex breakdown. However, in the stratified region, the magnitude of the angular velocity declines exponentially with distance from the lower plate, indicating that layering has a stronger effect on the transport of angular velocity compared to the more well-studied phenomenon of vortex-breakdown. The heat transfer coefficient was also found to decrease sharply upon the onset of the layering structure implying that the latter acts to insulate the top plate.

The study demonstrates that thermal gradients can control the flow in rotating equipment and have the potential to reduce power requirements albeit at the expense of heat transfer. Hence, the performance of such systems needs to be optimized for a given application. The GITT approach implemented in this study is very amenable to optimization problems due to its hybrid numerical-analytical nature and its efficiency relative to purely numerical techniques. This feature is inherent to hybrid numerical-analytical approaches, such as in the broad class of spectral methods, since the time consuming and approximate numerical task is associated with one single independent variable. Besides, the obtained hybrid solution can be exactly operated in those variables that have been eliminated through integral transformation, without any further approximation related to numerical differentiation or integration, and can be computed at specific positions and regions directly employing the inverse formulae, without requiring the numerical computation of the solution at a full mesh of nodes covering the entire physical domain. For the current problem, optimization in terms of either torque coefficient or heat transfer can be easily implemented through the corresponding analytical expressions derived (Eqs. (52) and (57), respectively).

It should be recalled that the present findings were based on two-dimensional simulations that assume the flow to be axisymmetric. However, the GITT methodology can be extended to explore the non-axisymmetric instabilities (i.e. 3D, unsteady breakdown) and their interaction with mixed convection.

Acknowledgements

JNNQ would like to acknowledge the financial support provided by the Brazilian sponsoring agencies CAPES and CNPq, and RMC the Leverhulme Trust Visiting Professorship (VP1-2017-028), respectively, as well as the kind hospitality of the Department of Mechanical Engineering, University College London (UCL), UK. This work was also partially supported by CNPq and FAPERJ, both research sponsoring agencies in Brazil.

References

- [1] Hall, M. G., 1972. "Vortex Breakdown". *Annual Review of Fluid Mechanics*, **4**, pp. 195-218.
- [2] Leibovich, S., 1978. "The Structure of Vortex Breakdown". *Annual Review of Fluid Mechanics*, **10**, pp. 221-246.
- [3] Escudier, M. P., 1988. "Vortex Breakdown: Observations and Explanations". *Progress in Aerospace Sciences*, **25**, pp. 189-229.
- [4] Delery, J. M., 1994. "Aspects of Vortex Breakdown". *Progress in Aerospace Sciences*, **30**, pp. 1-59.
- [5] Lucca-Negro, O., and O'Doherty, T., 2001. "Vortex Breakdown: A Review". *Progress in Energy and Combustion Science*, **27**, pp. 431-481.
- [6] Escudier, M. P., 1984. "Observations of the Flow Produced in a Cylindrical Container by a Rotating Endwall". *Experiments in Fluids*, **2**, pp. 189-196.
- [7] Jones, M. C., Hourigan, K., and Thompson, M. C., 2015. "A Study of the Geometry and Parameter Dependence of Vortex Breakdown". *Physics of Fluids*, **27**, pp. 044102-1-044102-13.
- [8] Serre, E. and Bontoux, P., 2002. "Vortex Breakdown in a Three-dimensional Swirling Flow". *Journal of Fluid Mechanics*, **459**, pp. 347-370.
- [9] Lugt, H. J., and Abboud, M., 1987. "Axisymmetric Vortex Breakdown with and without Temperature Effects in a Container with a Rotating Lid". *Journal of Fluid Mechanics*, **179**, pp. 179-200.
- [10] Brown, G. L., and Lopez, J. M., 1990. "Axisymmetric Vortex Breakdown Part 2. Physical Mechanisms". *Journal of Fluid Mechanics*, **221**, pp. 553-576.
- [11] Sørensen, J. N., Naumov, I., & Mikkelsen, R., 2006. "Experimental Investigation of Three-Dimensional Flow Instabilities in a Rotating Lid-Driven Cavity". *Experiments in Fluids*, **41**(3), pp.425-440.
- [12] Herrada, M. A., and Shtern, V., 2003. "Vortex breakdown Control by Adding Near-axis Swirl and Temperature Gradients". *Physical Review E*, **68**, pp. 041202-1-041202-8.

- [13] Dash, S. C., and Singh, N., 2018. "Stability Boundaries for Vortex Breakdowns and Boundaries Between Oscillatory and Steady Swirling Flow in a Cylindrical Annulus with a Top Rotating Lid". *Journal of the Brazilian Society of Mechanical Sciences and Engineering*, **40**, pp. 336-1-336-19.
- [14] Tan, B. T., Liow, K. Y. S., Mununga, L., Thompson, M. C., and Hourigan, K., 2009. "Simulation of the Control of Vortex Breakdown in a Closed Cylinder Using a Small Rotating Disk". *Physics of Fluids*, **21**, pp. 024104-1-024104-8.
- [15] Bessaih, R., Boukhari, A., and Marty, P., 2009. "Magnetohydrodynamics Stability of a Rotating Flow with Heat Transfer". *International Communications in Heat and Mass Transfer*, **36**, pp. 893-901.
- [16] Yu, Y., Li, B.-W., and Thess, A., 2013. "The Effect of a Uniform Magnetic Field on Vortex Breakdown in a Cylinder with Rotating Upper Lid". *Computers & Fluids*, **88**, pp. 510-523.
- [17] Ismadi, M.-Z. P., Meunier, P., Fouras, A., and Hourigan, K., 2011. "Experimental Control of Vortex Breakdown by Density Effects". *Physics of Fluids*, **23**, pp. 034104-1-034104-9.
- [18] Iwatsu, R., and Hyun, J. M., 1995. "Three-dimensional Driven-cavity Flows with a Vertical Temperature Gradient". *International Journal of Heat and Mass Transfer*, **38**, pp. 3319-3328.
- [19] Herrada, M. A., and Shtern, V., 2003. "Control of Vortex Breakdown by Temperature Gradients". *Physics of Fluids*, **15**, pp. 3468-3477.
- [20] Iwatsu, R., 2004. "Flow Pattern and Heat Transfer of Swirling Flows in Cylindrical Container with Rotating Top and Stable Temperature Gradient". *International Journal of Heat and Mass Transfer*, **47**, pp. 2755-2767.
- [21] Omi, Y., and Iwatsu, R., 2005. "Numerical Study of Swirling Flows in Cylindrical Container with Co-/Counter-Rotating End Disks under Stable Temperature Difference". *International Journal of Heat and Mass Transfer*, **48**, pp. 4854-4866.
- [22] Dash, S. C., and Singh, N., 2016. "Effects of Partial Heating of Top Rotating Lid with Axial Temperature Gradient on Vortex Breakdown in Case of Axisymmetric Stratified Lid Driven Swirling Flow". *Journal of Thermal Engineering*, **2**, pp. 882-896.
- [23] Turan, O., Yigit, S., and Chakraborty, N., 2018. "Effects of Wall Heating on Laminar Mixed Convection in a Cylindrical Enclosure with a Rotating End Wall". *International Journal of Thermal Sciences*, **131**, pp. 80-93.
- [24] Hart, J., Bhuiyan, A. A., and Naser, J., 2018. "Aerodynamics of burner jet in a tangentially-fired boiler: A CFD modelling and experiment". *International Journal of Thermal Sciences*, **129**, pp. 238-253.
- [25] Wan, H., Gao, Z., Ji, J., Fang, J., and Zhang, Y., 2019. "Experimental study on horizontal gas temperature distribution of two propane diffusion flames impinging on an unconfined ceiling". *International Journal of Thermal Sciences*, **136**, pp. 1-8.
- [26] Alekhin, V., Bianco, V., Khait, A., and Noskov, A., 2015. "Numerical investigation of a double-circuit Ranque-Hilsch vortex tube". *International Journal of Thermal Sciences*, **89**, pp. 272-282.

- [27] Lagrandeur, J., Poncet, S., and Sorin, M., 2019. "Review of predictive models for the design of counterflow vortex tubes working with perfect gas". *International Journal of Thermal Sciences*, **142**, pp. 188-204.
- [28] Lee, C. H., and Hyun, J. M., 1999. "Flow of a Stratified in a Cylinder with a Rotating Lid". *International Journal of Heat and Fluid Flow*, **20**, pp. 26-33.
- [29] Cui, Y. D., Lopez, J. M., Lim, T. T., and Marques, F., 2009. "Harmonically Forced Enclosed Swirling Flow". *Physics of Fluids*, **21**, pp. 034106-1-034106-11.
- [30] Mahfoud, B., and Bessaih, R., 2012. "Oscillatory Swirling Flows in a Cylindrical Enclosure with Co-/Counter-Rotating End Disks Submitted to a Vertical Temperature Gradient". *Fluid Dynamics & Materials Processing*, **8**, pp. 1-26.
- [31] Cotta, R. M., 1993. *Integral Transforms in Computational Heat and Fluid Flow*, CRC Press, Boca Raton.
- [32] Perez Guerrero, J.S., and Cotta, R.M., 1992, "Integral transform solution for the lid-driven cavity flow problem in streamfunction-only formulation". *Int. J. Num. Meth. in Fluids*, **15**, pp. 399 - 409.
- [33] Perez Guerrero, J.S., and Cotta, R.M., 1996, "Benchmark Integral Transform Results for Flow Over a Backward - Facing Step". *Computers & Fluids*, **25**, no.5, pp.527-540.
- [34] Leal, M.A., Machado, H.A., and Cotta, R.M., 2000, "Integral Transform Solutions of Transient Natural Convection in Enclosures with Variable Fluid Properties". *Int. J. Heat & Mass Transfer*, **43**, no.21, pp.3977-3990.
- [35] Ramos, R., Perez Guerrero, J.S., and Cotta, R.M., 2001, "Stratified Flow Over a Backward Facing Step:- Hybrid Solution by Integral Transforms". *Int. J. Num. Meth. in Fluids*, **35**, no.2, pp.173-197.
- [36] Matt, C.F.T., Quaresma, J.N.N., and Cotta, R.M., 2017, "Analysis of Magnetohydrodynamic Natural Convection in Closed Cavities through Integral Transforms". *Int. J. Heat & Mass Transfer*, **113**, pp.502-513.
- [37] Pereira, L. M., Perez-Guerrero, J. S., and Cotta, R. M., 2000. "Analysis of Laminar Forced Convection in Annular Ducts Using Integral Transforms". *Hybrid Methods in Engineering*, **2**, pp. 221-232.
- [38] Pereira, L. M., Perez-Guerrero, J. S., Brazão, N., and Cotta, R. M., 2002. "Compressible Flow and Heat Transfer in Ultracentrifuges: Hybrid Analysis via Integral Transforms". *International Journal of Heat and Mass Transfer*, **45**, pp. 99-112.
- [39] Pereira, L. M., Perez-Guerrero, J. S., and Cotta, R. M., 1998. "Integral Transformation of the Navier-Stokes Equations in Cylindrical Geometry". *Computational Mechanics*, **21**, pp. 60-70.
- [40] Silva, C. A. M., Macêdo, E. N., Quaresma, J. N. N., Pereira, L. M., and Cotta, R. M., 2010. "Integral Transform Solution of the Navier-Stokes Equations in Full Cylindrical Regions with Streamfunction Formulation". *International Journal of Numerical Methods in Biomedical Engineering*, **26**, pp. 1417-1434.

[41] IMSL® Fortran Numerical Library, 2018. Version 2018, Rogue Wave Software Inc., Boulder, USA.

Table 1

Number of the grid points in the final mesh obtained with the subroutine DBVFPD from the IMSL Library [41].

Test Case	Ri=0	Ri=0.1	Ri=1
Re=1492, h=1.5	NFinal=203	NFinal=203	NFinal=323
Re=2126, h=2.5	NFinal=425	NFinal=425	NFinal=425
Re=3061, h=3.5	NFinal=222	NFinal=254	NFinal=405

NFinal=Number of grid points.

Figure Captions:

Fig. 1. Geometric configuration of the mixed convection heat transfer problem in a cylindrical cavity with the rotating bottom end.

Fig. 2. Validation of the present GITT results (left) against the flow visualizations of Escudier⁶ (right): (a) $Re=1492$ and $h=1.5$; (b) $Re=2126$ and $h=2.5$; (c) $Re=3061$ and $h=3.5$.

Fig. 3. Verification of the present GITT results for the average Nusselt number against the numerical results of Omi and Iwatsu [21] for $Re=1000$ and $h=2$.

Fig. 4. Isolines of streamfunction, temperature and azimuthal vorticity for different Richardson numbers and $Re=1492$ and $h=1.5$: (a) $Ri=0$; (b) $Ri=0.01$; (c) $Ri=0.02$; (d) $Ri=0.1$.

Fig. 5. Flow transitions for progressively increasing Richardson numbers for the single bubble VB case ($Re=1492$ and $h=1.5$).

Fig. 6. Flow transitions for progressively increasing Richardson numbers for the double bubble VB case ($Re=2126$ and $h=2.5$).

Fig. 7. Flow transitions for progressively increasing Richardson numbers for the triple bubble VB case ($Re=3061$ and $h=3.5$).

Fig. 8. Effect of Richardson number on the number of flow stratification layers formed.

Fig. 9. Effect of Richardson number on the torque coefficient: a) variation of torque coefficient in the three VB cases with Ri ; b) reduced torque coefficient with an empirical power law fit for all cases.

Fig. 10. Distribution of absolute value of the mean azimuthal velocity, for the triple bubble VB case ($Re = 3061$, $h = 3.5$). The profiles correspond to the flow fields shown in Fig. 7.

Fig. 11. Effect of the Richardson number on the average Nusselt number.

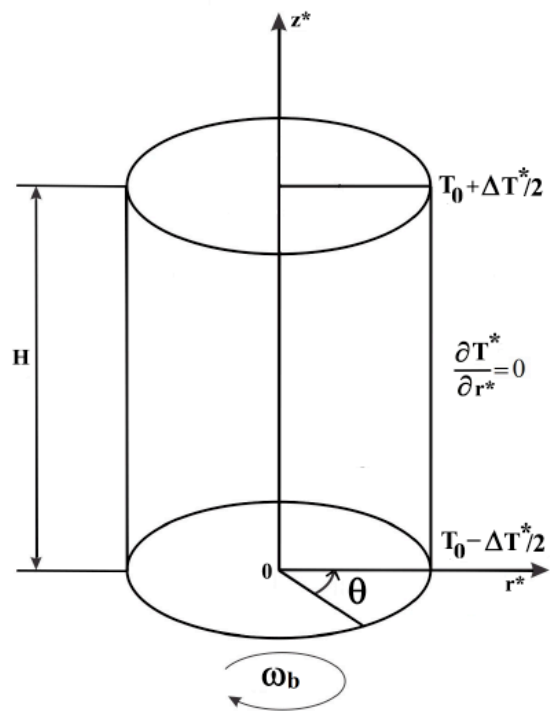
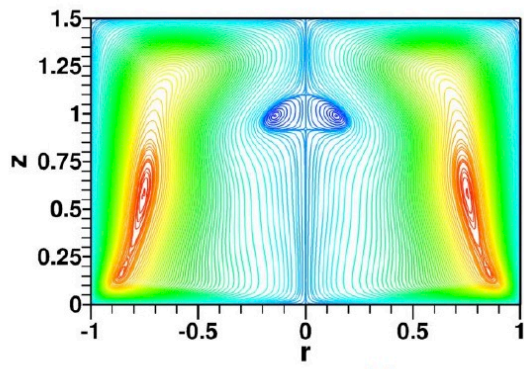
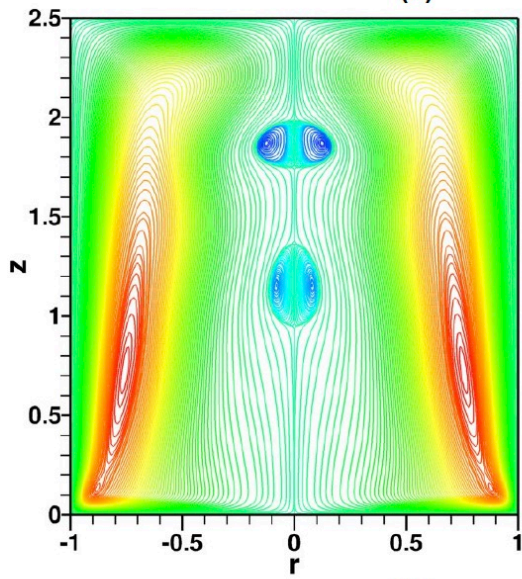


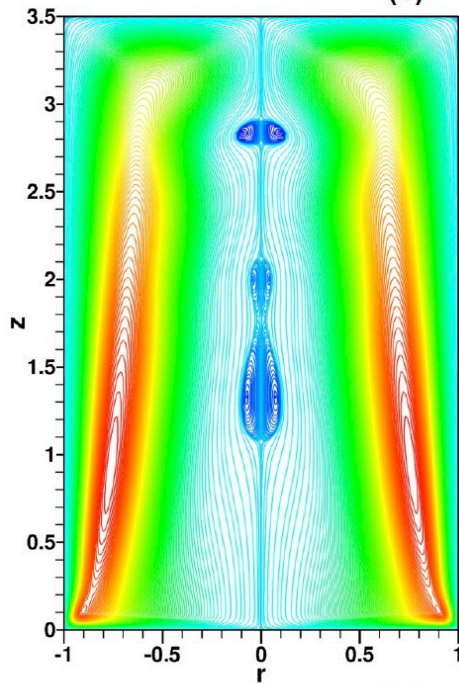
Fig. 1.



(a)



(b)



(c)

Fig. 2.

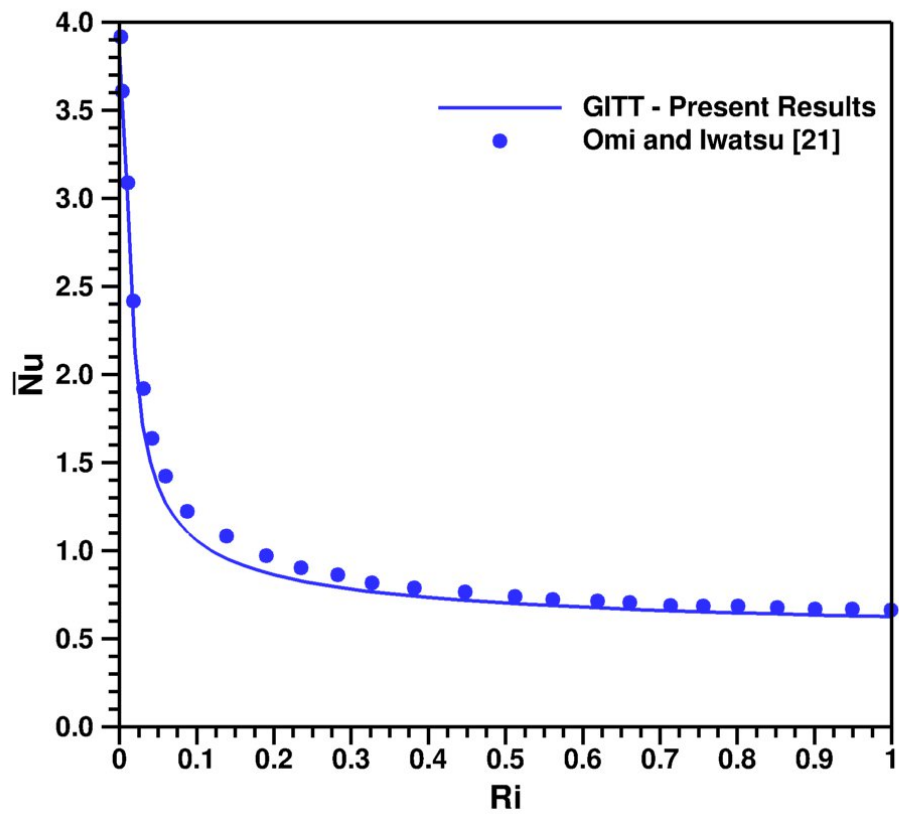


Fig. 3.

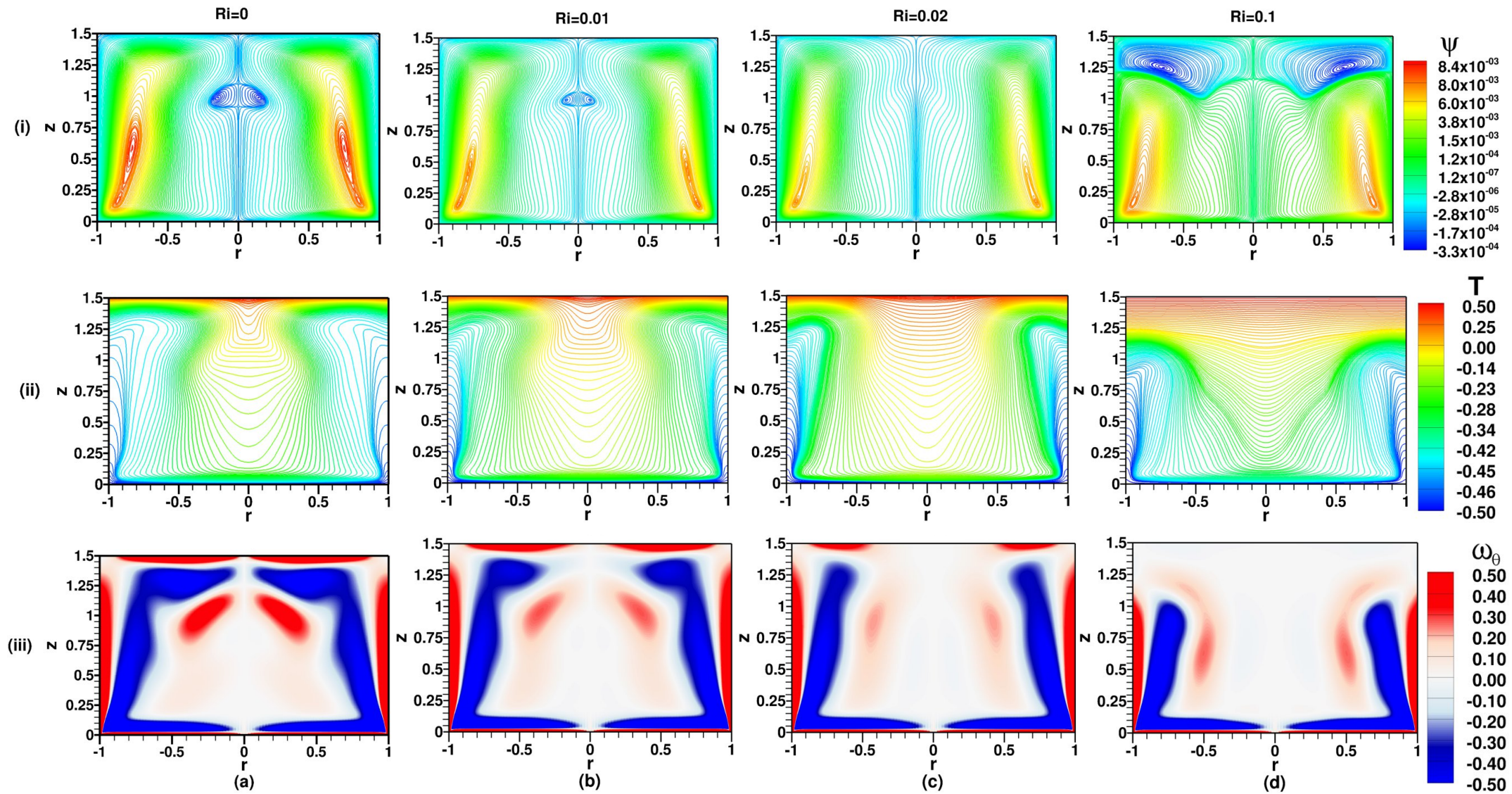


Fig. 4.

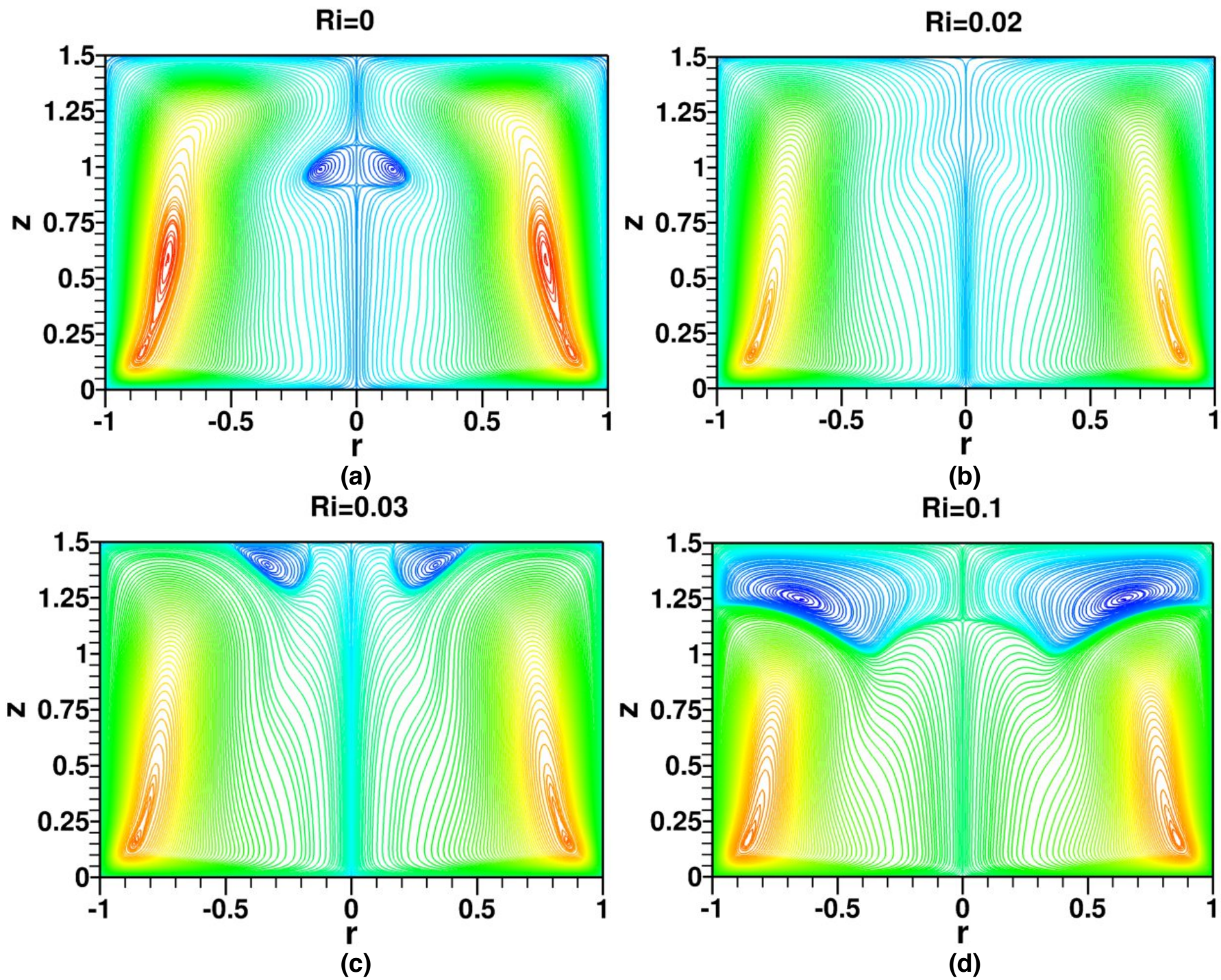


Fig. 5.

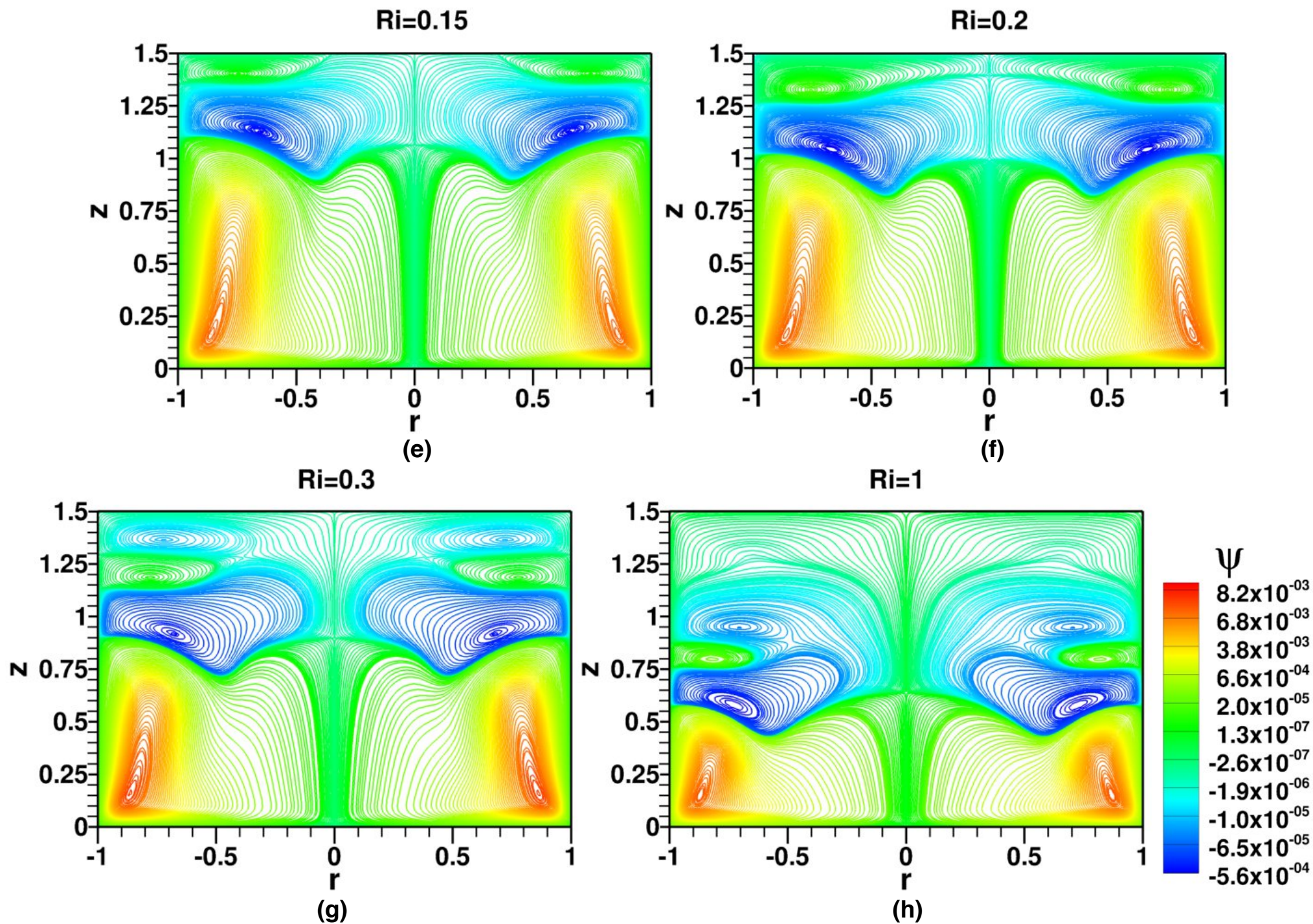


Fig. 5. Continued.

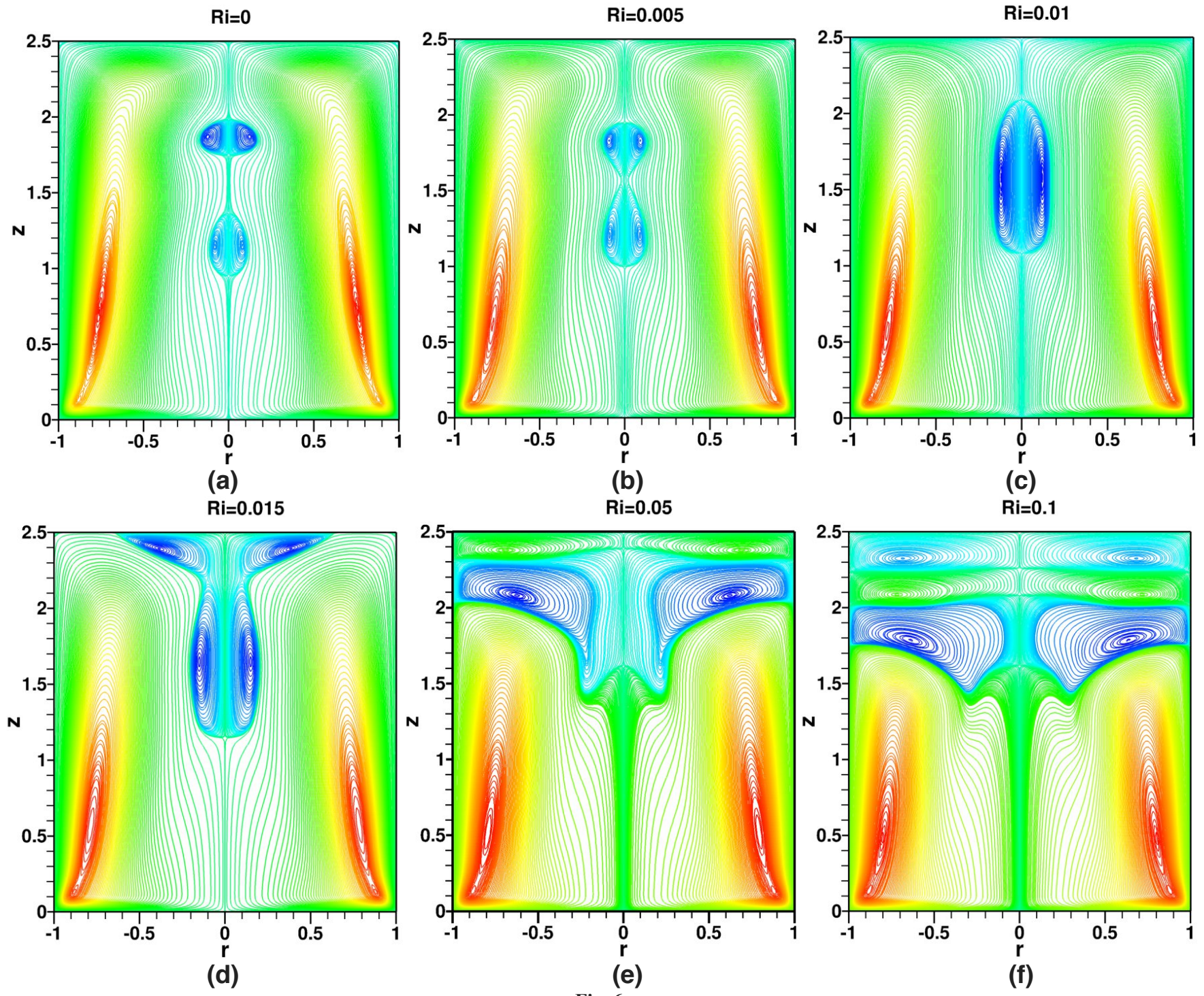
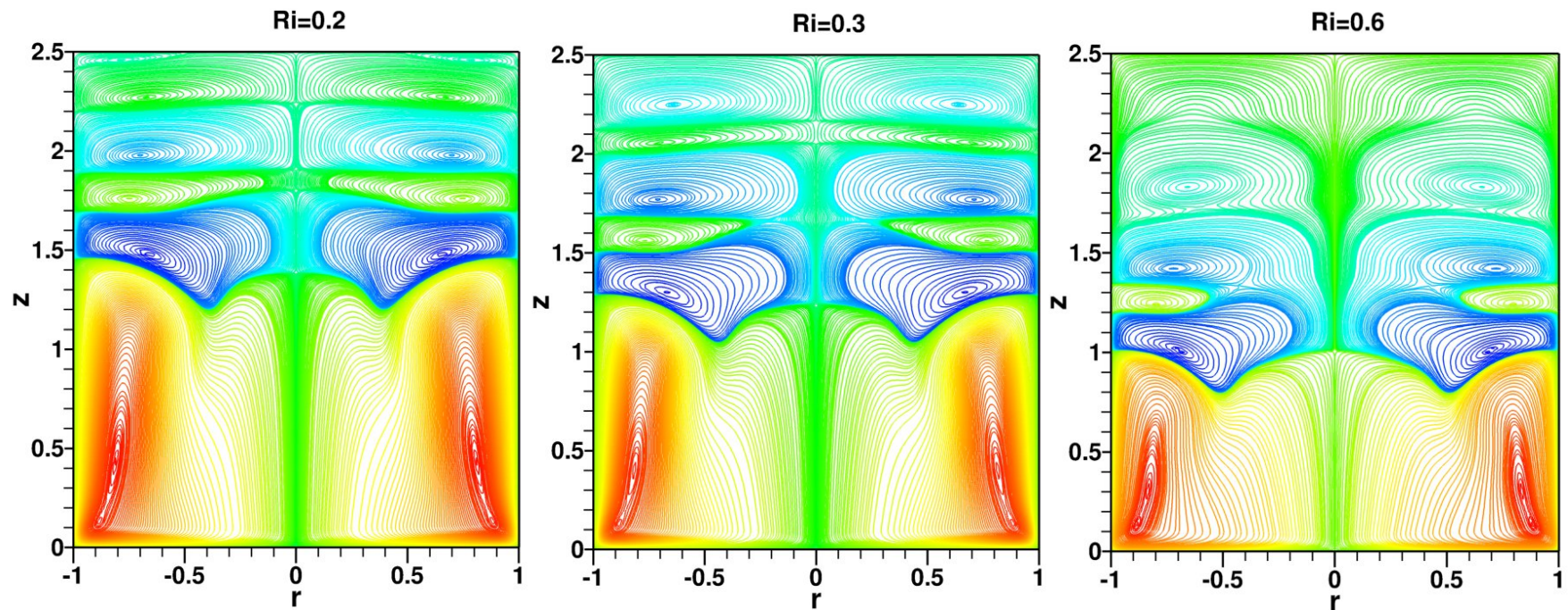


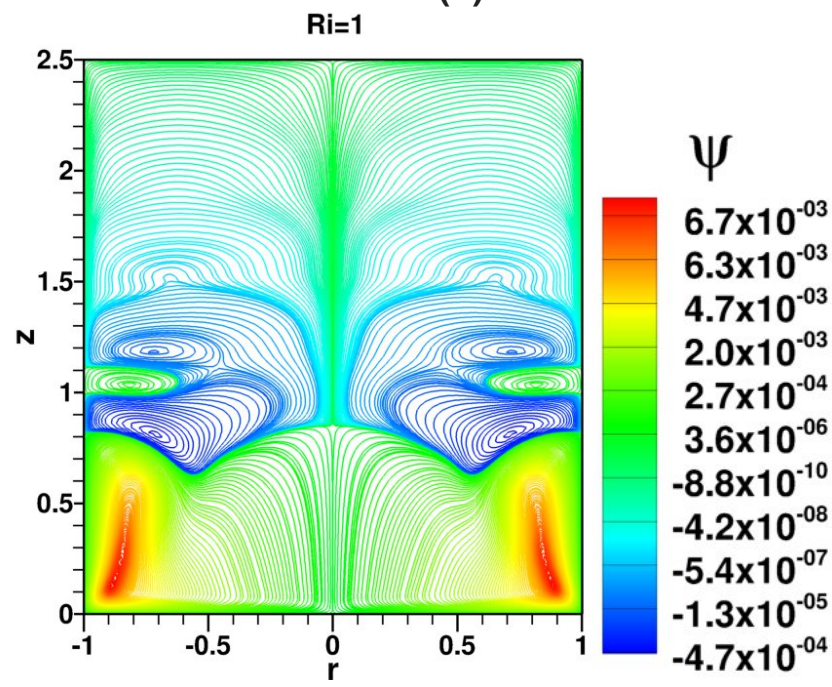
Fig. 6.



(g)

(h)

(i)



(j)

Fig. 6. Continued.

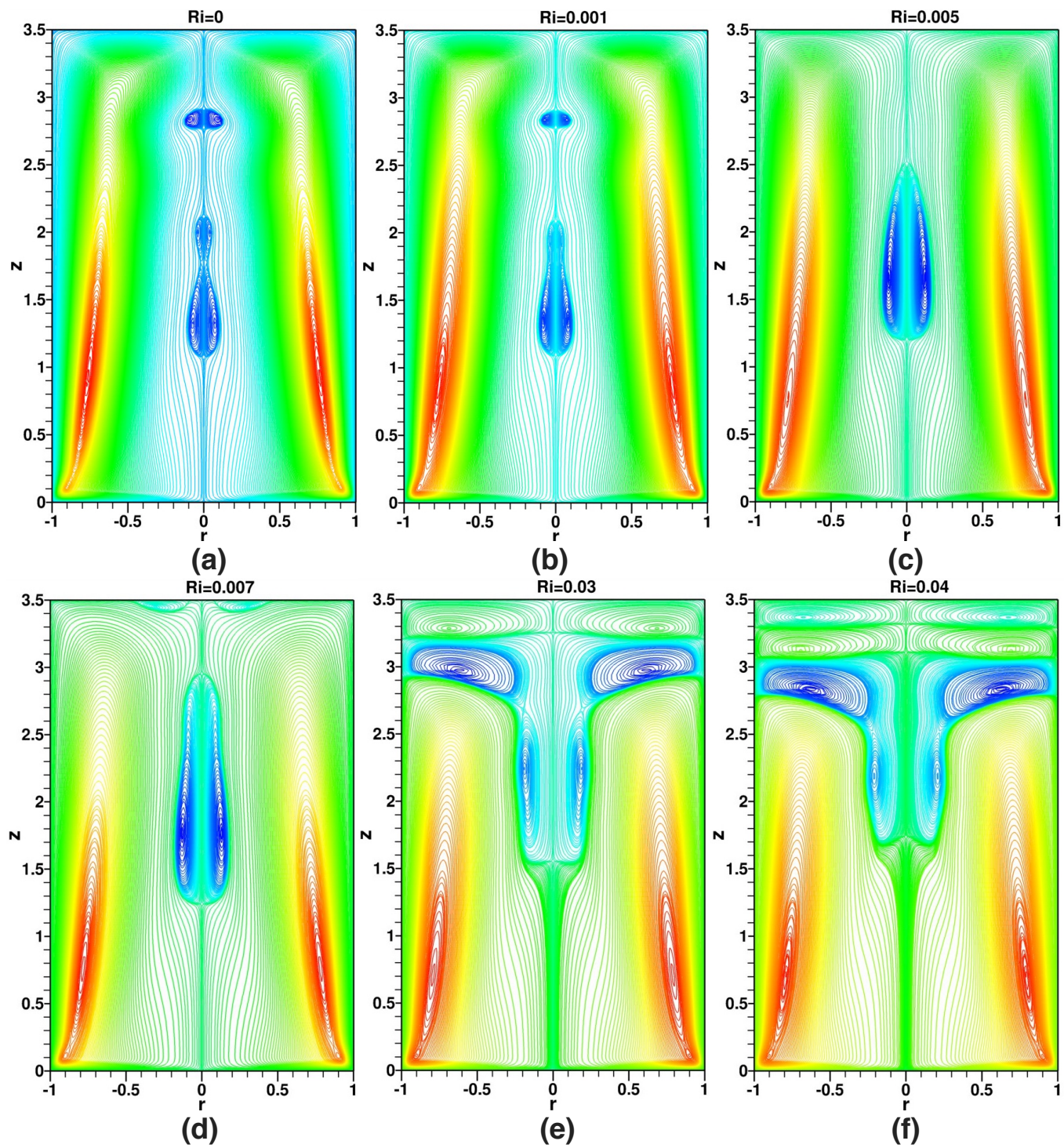


Fig. 7.

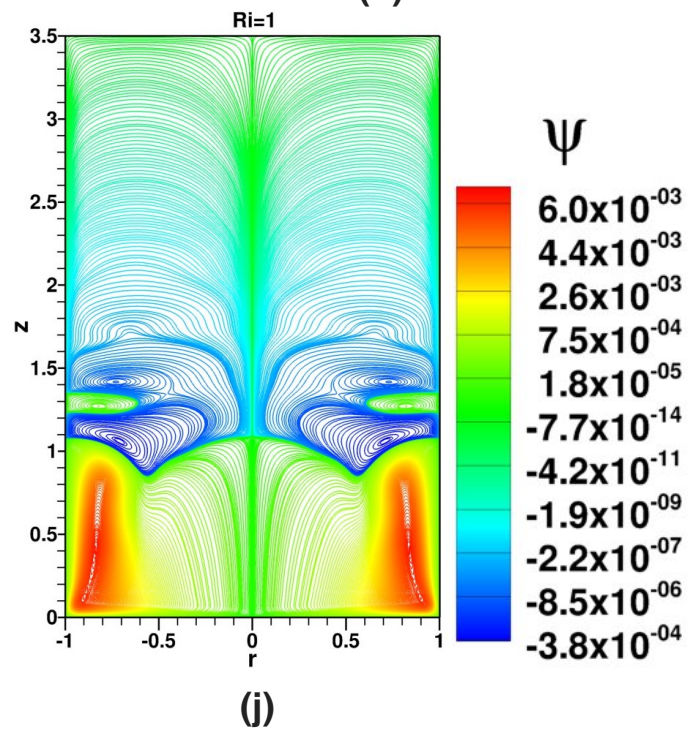
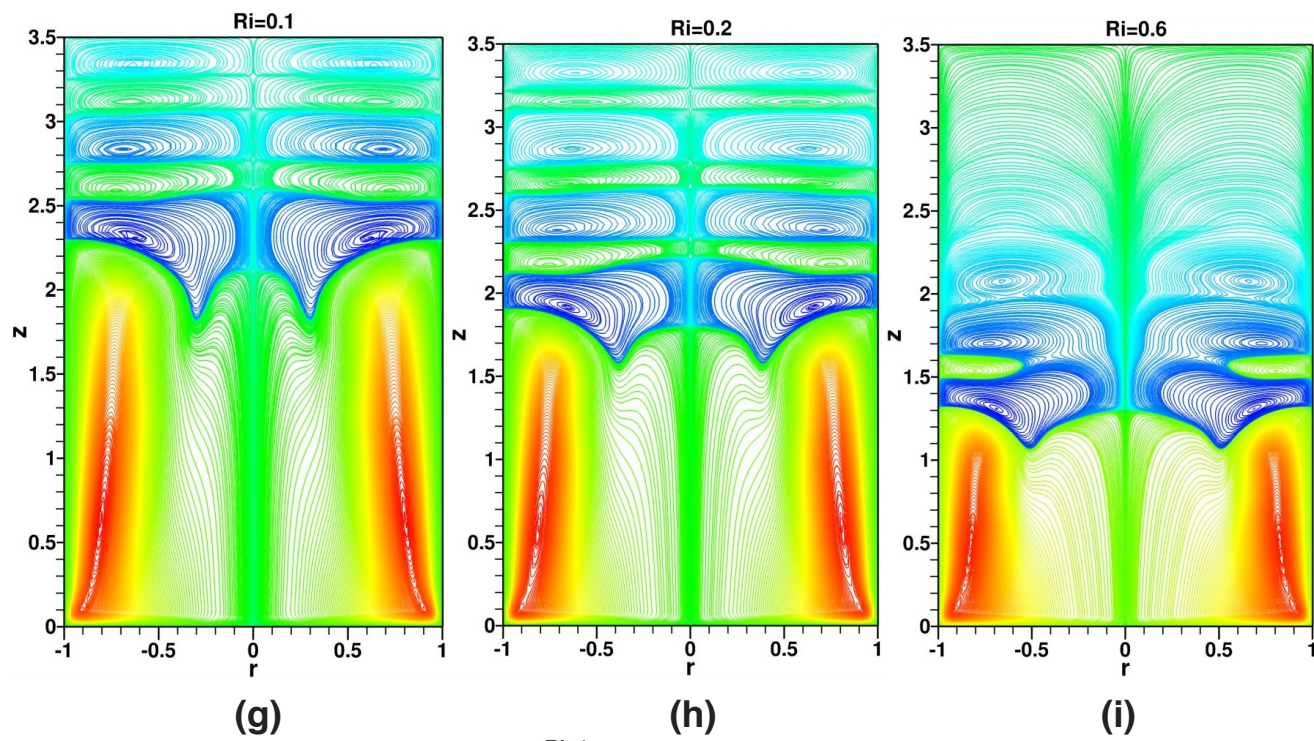


Fig. 7. Continued.

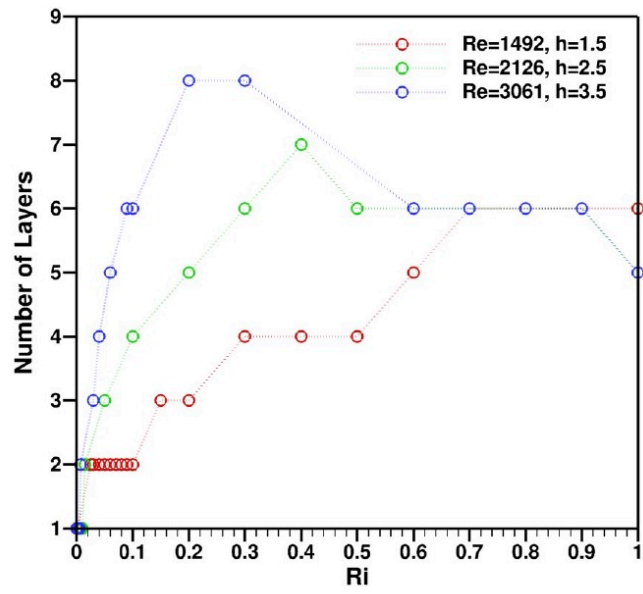


Fig. 8.

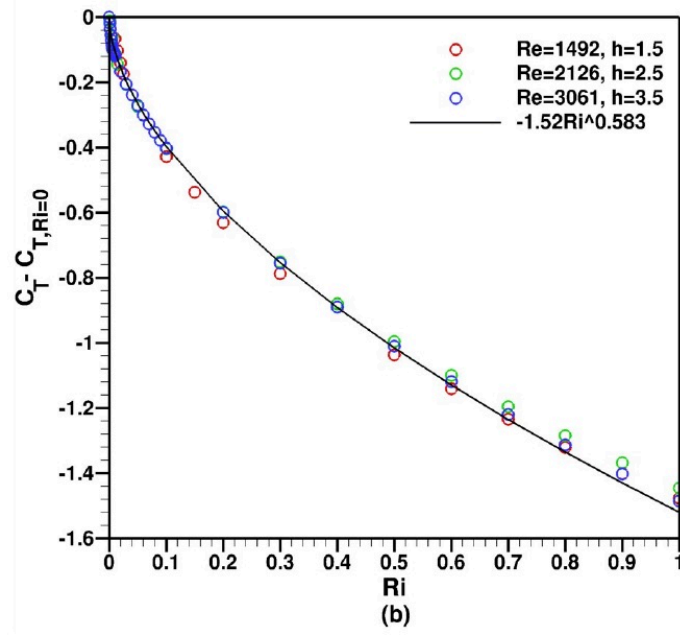
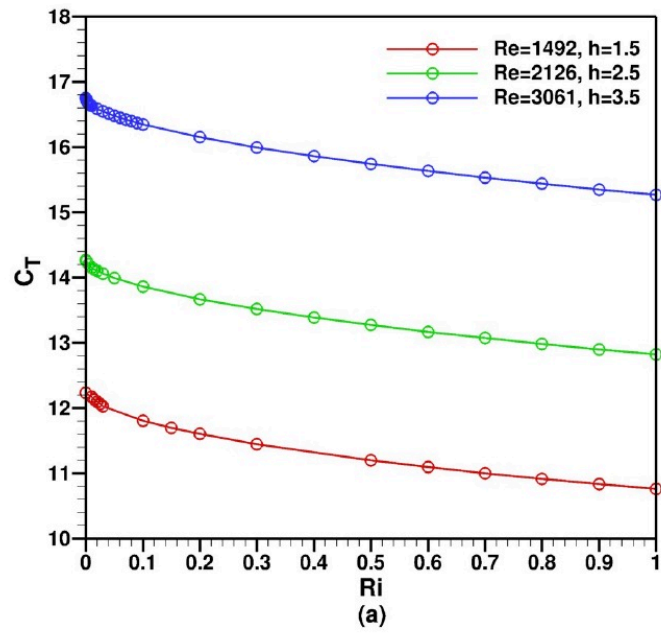


Fig. 9.

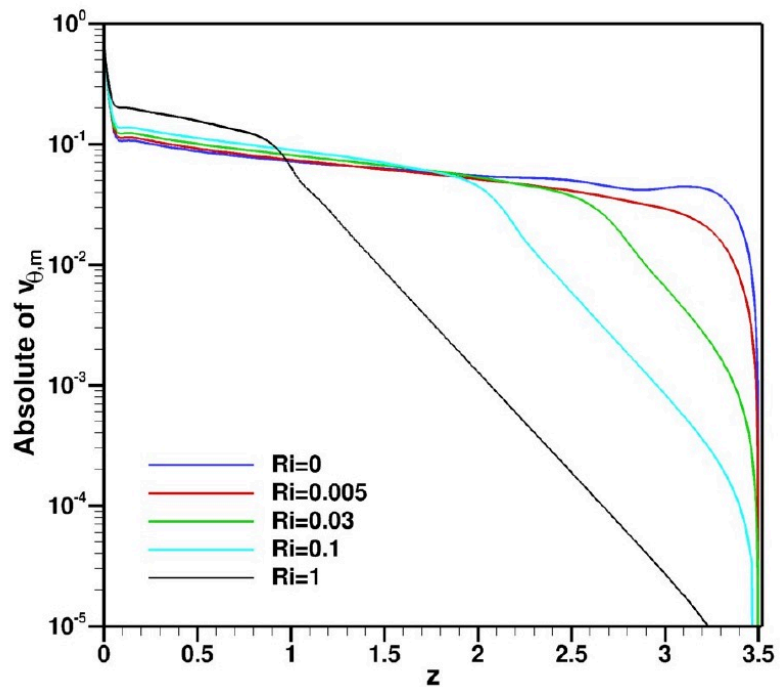


Fig. 10.

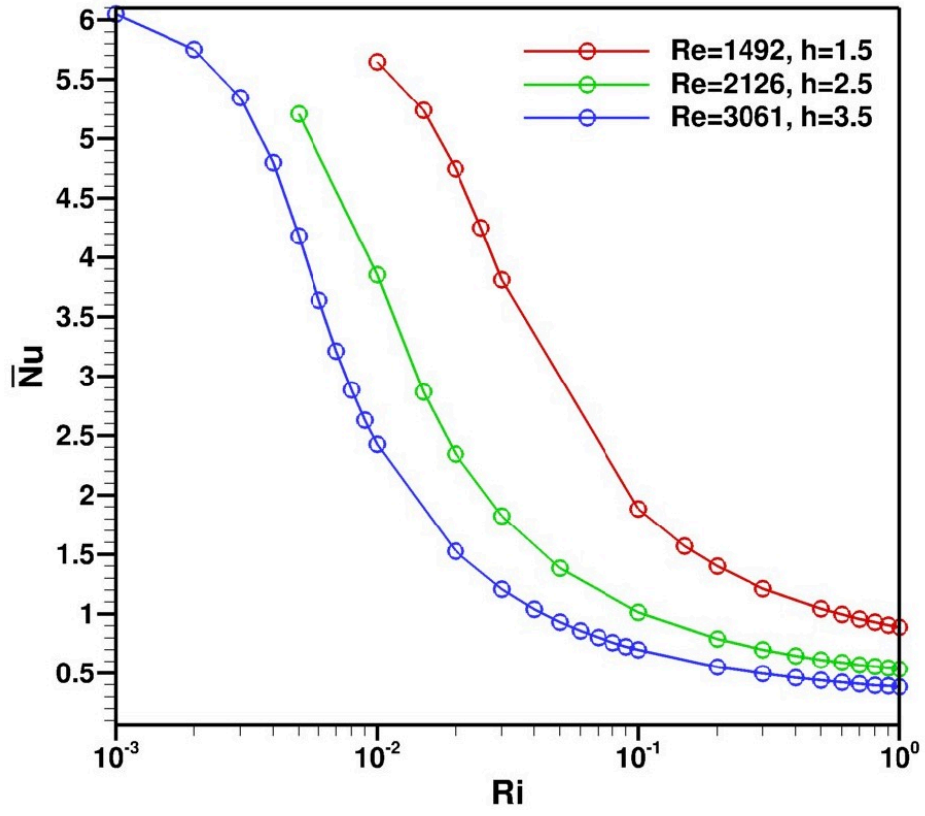


Fig. 11.